

1
2
3
4
5
6
7
8
9
10
11
12
13
14
15
16
17
18
19
20
21
22
23
24
25
26
27
28
29
30
31
32
33
34
35
36
37
38
39
40
41
42
43
44
45
46
47
48
49
50
51
52
53
54
55
56
57
58

Q1 Applicability of InSAR to tropical volcanoes: insights from Central America

S. K. EBMEIER^{1*}, J. BIGGS^{2,3}, T. A. MATHER¹ & F. AMELUNG³

¹COMET+, Department of Earth Sciences, University of Oxford,
South Parks Road, Oxford OX1 3AN, UK

²COMET+, Department of Earth Sciences, University of Bristol, Wills Memorial
Building, Queens Road, Bristol BS8 1RJ, UK

³RSMAS, University of Miami, 4600 Rickenbacker Causeway, Miami, FL 33149, USA

*Corresponding author (e-mail: susanna.ebmeier@earth.ox.ac.uk)

Abstract: Measuring volcano deformation is key to understanding the behaviour of erupting volcanoes and detecting those in periods of unrest. Satellite techniques provide the opportunity to do so on a global scale but, with some notable exceptions, the deformation of volcanoes in the tropics has been understudied relative to those at higher latitudes, largely due to technical difficulties in applying Interferometric Synthetic Aperture Radar (InSAR).

We perform a systematic survey of the Central American Volcanic Arc to investigate the applicability of Interferometric Synthetic Aperture Radar (InSAR) to volcanoes in the tropics. Volcano characteristics that may prevent InSAR measurement include: (1) dense vegetation cover; (2) persistent activity; and (3) steep slopes. Measurements of deformation are further inhibited by atmospheric artefacts associated with: (4) large changes in topographical relief. We present a systematic method for distinguishing between water vapour artefacts and true deformation. Our data show a linear relationship (*c.* 2 cm/km) between the magnitudes of water vapour artefacts and volcano edifice height. For high relief volcanoes (e.g. Fuego, Guatemala, 3763 m a.s.l. (above sea level)) errors are of the order of 4–5 cm across the volcano's edifice but are less than 2 cm for lower relief (e.g. Masaya, Nicaragua, 635 m a.s.l.). Examples such as Arenal, Atitlan and Fuego illustrate that satellite acquisition strategies incorporating ascending and descending tracks are particularly important for studying steep-sided volcanoes.

Poor coherence is primarily associated with temporal decorrelation, which is typically more rapid in southern Central America where Evergreen broad-leaf vegetation dominates. Land-use classification is a better predictor of decorrelation rate than vegetation index. Comparison of coherence for difference radar wavelengths match expectations; high resolution X-band radar is best suited to local studies where high-resolution digital elevation models (DEMs) exist, while L-band wavelengths are necessary for regional surveys. However, this

is the first time that relationships between phase coherence and time, perpendicular baseline, radar wavelength, and land use have been quantified on the scale of a whole volcanic arc.

Interferometric synthetic aperture radar has been used to detect and measure deformation at over 70 volcanoes worldwide since the 1990s (Fournier *et al.* 2010). A variety of different types of deformation have been observed using InSAR surveys, including the movement of magma during co-eruptive deformation (e.g. Lu & Dzurisin 2010) or intrusive processes (e.g. dyke and sill intrusion: Hamling *et al.* 2009; Biggs *et al.* 2010), as well as a variety of shallower surface processes. These include hydrothermal activity (Pritchard & Simons 2004), slow edifice subsidence (Ebmeier *et al.* 2010) and lava flow contraction (Stevens *et al.* 2001). Regional-scale surveys have detected magma movement at volcanoes previously thought to be quiescent (e.g. on the East African Rift: Biggs *et al.* 2009) and at locations not obviously associated with a particular volcanic edifice (e.g. the central Andes: Pritchard & Simons 2004).

However, the global distribution of InSAR measurements of volcano deformation is currently uneven, due, in part, to the differences in radar returns from different types of land surface. The majority of radar satellites have operated at C-band wavelengths, $\lambda = 5.6$ cm, which is known to be affected by vegetation cover. This is a particular problem in the tropics where dense, rapidly growing evergreen vegetation is especially prevalent and causes a high rate of change in surface scatterer properties and therefore rapid decorrelation. This

has presented significant obstacles for some C-band studies of volcano deformation in the tropics (Zebker *et al.* 2000; Stevens & Wadge 2004; Pinel *et al.* 2011). In recent years, this problem has been addressed to some extent with the launch of the Japanese satellite, ALOS, in 2006, which operates at L-band ($\lambda = 23$ cm) wavelengths. L-band radar penetrates dense vegetation so that the radar returns come from more stable scatterers on the ground surface. ALOS (Advanced Land Observing Satellite) data have allowed the first InSAR measurements at many volcanoes in the Caribbean, northern Andes, Indonesia and Central America (Biggs *et al.* 2010; Ebmeier *et al.* 2010; Fournier *et al.* 2010; Parks *et al.* 2010; Philibosian & Simons, 2011). Nonetheless, since the C-band archive stretches back to 1993 while ALOS was only launched in 2006, heavily vegetated volcanoes, many of which are in the tropics, have been under-studied relative in drier regions.

Many of the world's active volcanoes are in the tropics and have little or no coverage by ground-based geodetic measurement (e.g. Fournier *et al.* 2009), so that InSAR observations may be the only available method for assessing and monitoring their geodetic activity and the related volcanic hazard. It is therefore important from both hazard mitigation and satellite design perspectives to quantify the applicability of InSAR to tropical volcanoes.

In this study we explore the factors that affect the measurement of volcano deformation in the tropics using InSAR, drawing on examples from an L-band survey of the Central American Volcanic Arc (CAVA) between 2007 and 2010. Some of these factors apply globally (e.g. DEM quality) while others (water vapour variations, vegetation) are of particular concern at tropical volcanoes. We start by discussing the most significant issue, namely stratification and the variability in tropospheric water vapour concentration (see the section on 'Tropospheric water vapour' later), which creates artefacts over topographical peaks. Although such atmospheric artefacts are found at volcanoes across a wide range of latitudes, the significantly greater variability in water vapour concentrations in the tropics make them an extreme case. In the section on 'Limitations of global DEMs and mitigation' we discuss artefacts associated with the use of global DEMs in the section on 'Geometric distortion and optimal acquisition strategy', geometric distortion effects. In the section 'Coherence in Central America' we discuss patterns in phase decorrelation rates across the arc, and their relationship to vegetation indexes and land-use classifications, and compare the usefulness and coherence of C-, L- and X- band SAR for a case study volcano, Arenal. The significance of the lack of observations of volcano deformation in Central America in

relation to uncertainties in InSAR measurement and to tectonic setting is beyond the scope of the current study and is the focus for future work (Ebmeier *et al.* in prep).

InSAR

Repeat pass InSAR produces maps of phase change (interferograms) between two time-separated radar images from which the movement of the ground can be measured on the scale of millimetres to tens of centimetres (Massonet & Feigl 1998; Bürgmann *et al.* 2000). Phase shifts in an interferogram are caused by changes to satellite viewing geometry (satellite position and relative rotation of target between acquisitions, $\Delta\Phi_{\text{spatial}}$), instrument thermal noise ($\Delta\Phi_{\text{thermal}}$), radar path through the atmosphere ($\Delta\Phi_{\text{atm}}$) and backscatter from the ground surface. Changes at the Earth's surface capable of introducing phase shifts to an interferogram include deformation ($\Delta\Phi_{\text{def}}$), systematic changes to dielectric properties (e.g. due to moisture or thermal expansion/contraction, $\Delta\Phi_{\text{ground}}$) and changes to scattering properties within a pixel ($\Delta\Phi_{\text{pixel}}$). The scattering properties of a pixel are determined by the combination of radiation reflected or scattered from numerous objects, so that it has the appearance of random noise and cannot be predicted in practice.

$$\Delta\Phi = \Delta\Phi_{\text{spatial}} + \Delta\Phi_{\text{thermal}} + \Delta\Phi_{\text{atm}} + \Delta\Phi_{\text{def}} + \Delta\Phi_{\text{ground}} + \Delta\Phi_{\text{pixel}}. \quad (1)$$

Interferometric measurement of surface deformation ($\Delta\Phi_{\text{def}}$) is possible either when other sources of phase shift are relatively small or are constant over large areas.

The coherence of a pixel is usually described in terms of interferometric correlation ($\langle \rangle$), which is defined for each pixel using the phase values of both images (y_1 and y_2) across a square of at least 3×3 pixels (Equation 2). A value of 1 indicates identical phase for all pixels. When interferometric coherence tends to 0, each pixel response is independent (Seymour & Cumming 1994; Hanssen 2001):

$$|\hat{\gamma}| = \frac{|\sum_{n=1}^9 y_1^{(n)} y_2^{*(n)}|}{\sqrt{\sum_{n=1}^9 |y_1^{(n)}|^2 \sum_{n=1}^9 |y_2^{(n)}|^2}}. \quad (2)$$

Interferometric decorrelation is caused by changes in satellite position (geometric decorrelation), instrument properties (thermal decorrelation) and in surface scatterer characteristics (temporal decorrelation) (for further details see Zebker &

Q2

Q3

Q4

117 Villasenor 1992). Geometric decorrelation occurs
 118 where the radar wavelength is less than the differ-
 119 ence in path length between radar returns from
 120 opposite sides of a pixel, and is most pronounced
 121 at large baselines. Thermal decorrelation occurs
 122 when the behaviour of the satellite radar antenna
 123 varies over time. Temporal decorrelation is caused
 124 by scatterers within a pixel moving or changing
 125 their reflective properties. For satellite incidence
 126 angles of less than 45°, InSAR is more sensitive to
 127 vertical than horizontal changes to scatters, so that
 128 surfaces where volume scattering is significant
 129 (e.g. forests, dense vegetation) are expected to dec-
 130 orrelate more rapidly with time (Zebker & Villase-
 131 nor 1992). Precipitation, wind and ecological
 132 processes have all been observed to contribute to
 133 **Q5** temporal decorrelation (Ahmed 2011).

134 InSAR archive: the Central American 135 Volcanic Arc

136 The Central American Volcanic Arc stretches over
 137 1100 km from northern Guatemala, through El Sal-
 138 vador and Nicaragua to central Costa Rica, and is
 139 associated with the subduction of the Cocos Plate
 140 beneath the Caribbean Plate (Fig. 1). It is made up
 141 of 72 volcanoes, spaced at an average of approxi-
 142 mately 25 km along the arc (Carr 1984), of which
 143 26 are historically active.

144 Interferograms were produced from ALOS data
 145 between 2007 and 2010. All interferograms were
 146 constructed using the Repeat Orbit Processing soft-
 147 ware (ROI PAC) developed at Caltech/JPL (Rosen
 148 *et al.* 2004) with topographical correction made
 149 using NASA's Shuttle Radar Topography Mission
 150 (SRTM) 90 m DEM. Unwrapping was carried out
 151 using a branch-cut algorithm (Goldstein *et al.*
 152 1988) with corrections made manually. The volca-
 153 noes were covered by an average of 15 ascending
 154 interferograms, with a few supplementary descend-
 155 ing interferograms constructed where the ascend-
 156 ing data were ambiguous (Fig. 1). We were able to
 157 make geodetic measurements at 18 (Santa Maria
 158 (Santiaguito), Almolonga, Atitlan, Acatenango,
 159 Fuego, Pacaya, Santa Ana, Izalco, San Salvador,
 160 San Miguel, San Cristobal, Telica, Cerro Negro,
 161 Las Pilas, Momotombo, Masaya, Arenal and Poàs)
 162 of Central America's 26 active volcanoes and to
 163 characterize the associated uncertainty for each.

164 Tropospheric water vapour

165 *Water vapour characteristics*

166 In order to convert the observed phase changes to
 167 measurements of displacement, it is assumed that
 168 radar propagates at a constant velocity. This would

169 be reasonable for free space, where phase is depen-
 170 dent only on radar wavelength and path length, but
 171 introduces errors where there are significant spatial
 172 and temporal heterogeneities in the atmosphere.
 173 The effective path length actually depends on temp-
 174 erature, pressure and partial pressure of water
 175 vapour between satellite and ground surface, and is
 176 separated into 'wet' and 'hydrostatic' delays, caused
 177 by water vapour and hydrostatic pressure respec-
 178 tively (Bevis *et al.* 1992; Hanssen 2001). Water
 179 vapour artefacts in interferograms depend on the
 180 difference between atmospheric conditions on the
 181 two dates when Synthetic Aperture Radar (SAR) data
 182 were acquired. Variations in water vapour (e.g.
 183 10 cm path delay for a 20% change in relative humid-
 184 ity) are expected to produce larger path delays than
 185 hydrostatic pressure (2.3 mm path delay expected
 186 for change from 0.5 to 1 mb) (Zebker *et al.* 1997).

The spatial and temporal characteristics of the
 187 atmospheric artefacts depend on the distribution of
 188 water vapour in the troposphere. Where water
 189 vapour is mixed turbulently, it exhibits spatial cor-
 190 relation over length scales typically of the order of
 191 10 km (e.g. Hanssen 2001; Jónsson *et al.* 2002
 192 Lohman & Simons 2005), shows minimal or no cor-
 193 relation with topography and has a typical variabil-
 194 ity of 1 cm (e.g. Pritchard & Simons 2004). Large,
 195 steep volcanoes are commonly associated with both
 196 local turbulence on much smaller spatial scales and
 197 systematic features in atmospheric mixing caused
 198 by high topography (e.g. Webley (2004)).

Vertically stratified water vapour in the tropo-
 199 sphere results in low-magnitude slant range path
 200 delays over high topography and higher, more vari-
 201 able path delays over low topography (e.g. Pavez
 202 *et al.* (2006)). The resulting artefacts in an interfer-
 203 ogram correlate with topography, and appear as
 204 concentric fringes around topographical peaks
 205 (Fig. 2). As we may expect volume change of a sub-
 206 edifice magma chamber to produce a similar phase
 207 pattern, centred over the volcanic edifice (e.g. as
 208 observed at Etna: Massonnet *et al.* 1995; Beauducel
 209 *et al.* 2000), it is particularly difficult to distinguish
 210 between these two effects.

In equatorial zones, seasonal variations in water
 211 vapour are largely controlled by the north–south
 212 migration of the intertropical convergence zone
 213 (ITCZ), producing some of the greatest variations
 214 in water vapour globally. Radar path delays of up
 215 to 11, 8 and 6 cm have been measured at Mount
 216 Cameroon (Heleno *et al.* 2010), Sakurajima, Japan
 217 (Remy *et al.* 2003), and Soufrière Hills, Montserrat
 218 (Wadge *et al.* 2006), respectively (Table 1).

219 *Identification of atmospheric artefacts*

220 Characteristic features of atmospheric phase arte-
 221 facts include: (a) a correlation between topography

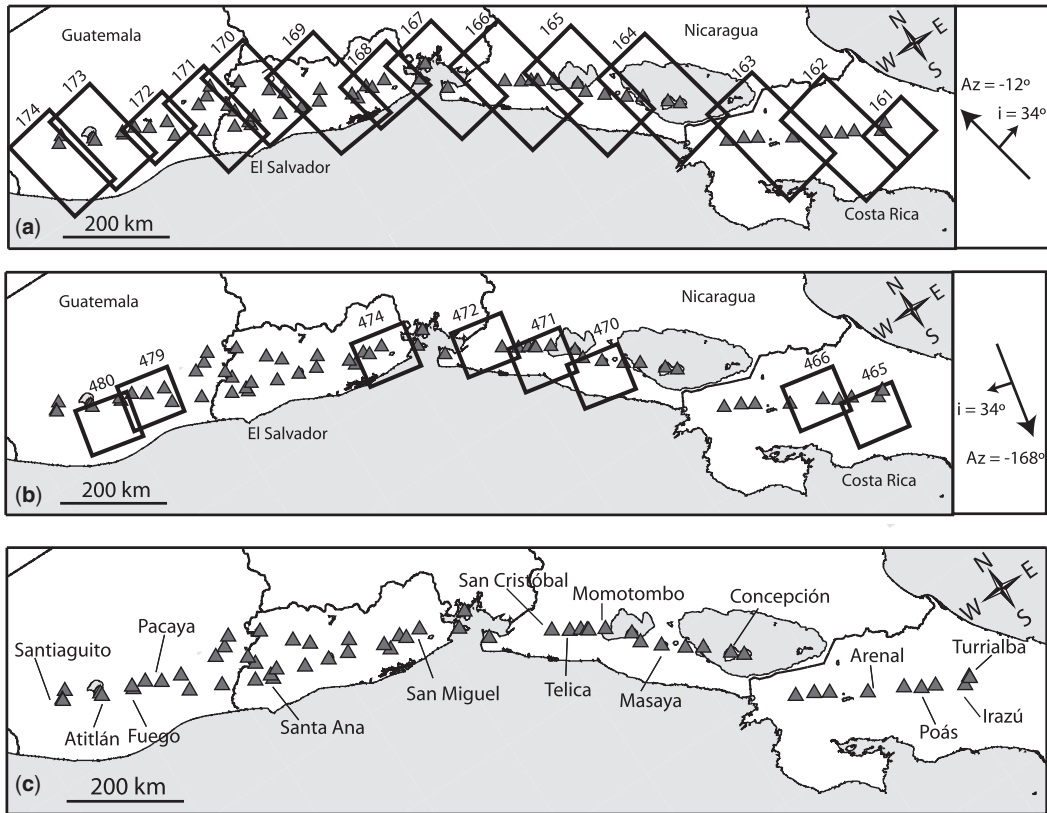


Fig. 1. (a) Ascending ALOS data used in arc-scale study of Central American Volcanic Arc. Black boxes show the track locations and extent of our data, and triangles show volcano locations. (b) Descending ALOS data used to complement ascending data where possible. (c) Map showing the locations of the volcanoes mentioned in this study.

and phase (for stratified water vapour); (b) an association of the signal with particular acquisition dates; and (c) either the lack of any dependence on time (turbulent water vapour) or a seasonal dependence (stratified water vapour) of signal magnitude (Fig. 3). Water vapour artefacts are identified using a combination of these properties, as well as through the use of independent atmospheric data or models (examples from the literature are shown in Table 1).

A correlation between height of topography and phase in an individual interferogram is indicative of the presence of water vapour (e.g. Fig. 4) but is not necessarily diagnostic. The injection or drainage of a body of magma within or just below a volcanic edifice could conceivably create a similar pattern in phase. However, where a number of topographical peaks in the same interferogram show similar phase patterns, they are most probably caused by atmospheric delay.

Analysis of the temporal development of phase through a set of interferograms provides further

evidence to distinguish between atmospheric artefacts and true deformation. The method of ‘pair-wise logic’ (e.g. Massonnet & Feigl 1995) compares pairs of interferograms that have a common date in master and slave positions. If artefacts of a similar magnitude and spatial pattern but opposite sign appear, then the artefact can be associated with the SAR acquisition date held in common. Two examples of such pairs from Momotombo Volcano, Nicaragua are shown in Figure 5. Although this method had the advantage of simplicity, it is only reliable where atmospheric conditions are relatively stable and unusual phase delays are associated with a small number of acquisition dates.

At the sampling rate of a satellite repeat intervals, we expect the temporal signal of atmospheric water vapour to be either structureless, with a random variation in phase between relatively constant bounds, or to vary with the period of a year as a function of seasonal variations in water vapour (e.g. Heleno *et al.* 2010). Creating time series of interferometric phase (e.g. Lundgren *et al.* 2001;

233
234
235
236
237
238
239
240
241
242
243
244
245
246
247
248
249
250
251
252
253
254
255
256
257
258
259
260
261
262
263
264
265
266
267
268
269
270
271
272
273
274
275
276
277
278
279
280
281
282
283
284
285
286
287
288
289
290

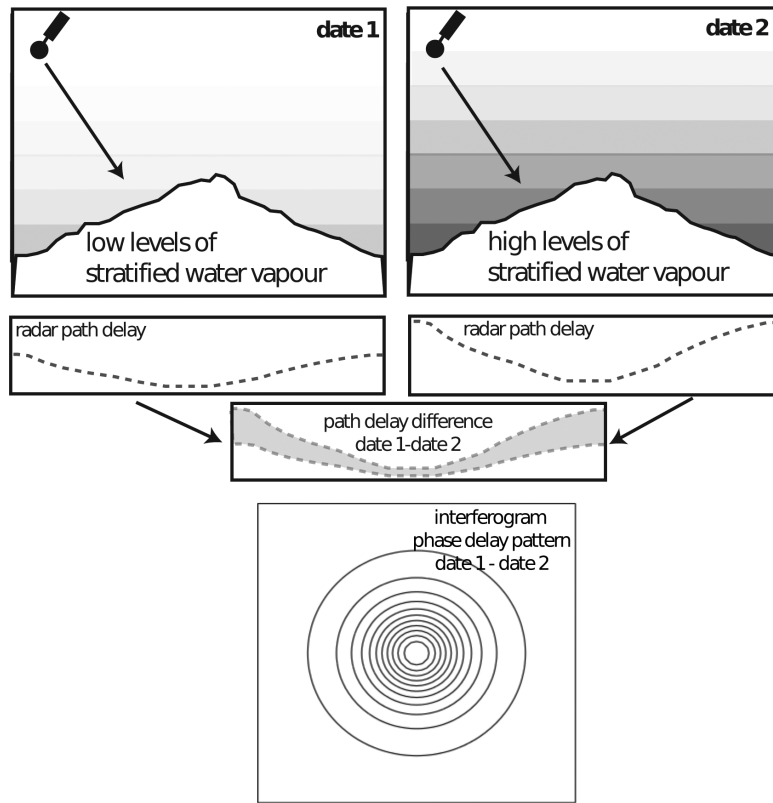


Fig. 2. Cartoon illustrating the generation of a topographically correlated phase delay due to variations in concentration of stratified water vapour. Typical values for peak phase delay range from 1 to 5 cm (2 cm would indicate *c.* 5% change in relative humidity).

Berardino *et al.* 2002) is a useful tool when dealing with situations where atmospheric effects seem to dominate the majority of interferograms. Long-term, steady-rate deformation may be detectable in this way (e.g. Ferretti *et al.* 2001), but reversible deformation (where net deformation over longer time-span interferograms will be zero, as the ground returns to its original position) may be missed.

InSAR only provides relative measurements, as phase changes are always found relative to a reference point. While for volcanoes it is generally possible to select a reference far away from any deformation source, it is very difficult to avoid the effects of local atmospheric variation. If a reference pixel is selected over an area where atmospheric variation differs to that over the volcano, local differences in atmospheric delay are likely to dominate time series and mask any deformation.

We avoid this problem by referencing our interferograms to the average value of phase within an annulus centred on the volcano, thus minimizing the impact of small-scale variations in atmospheric noise in other parts of the interferogram on our

time series. Reference annuli typically had inner radii of 2–6 km (large enough to encompass entire edifice and surrounding topographical features) and outer radii with limits defined by either the edge of the interferogram or (more commonly) the limit of the continuously coherent area. The difference between the mean height of topography within this area and the volcano summit was generally close to the volcano edifice height.

Water vapour in Central America

We use the characteristic properties described above and the processes outlined in Figure 3 to identify atmospheric water vapour in the Central American dataset. We constructed time series for active volcanoes in Central America using a linear least squares inversion of the phase changes from a network of interferograms (e.g. Lundgren 2001; Schmidt & Bürgmann 2003). Inversion was carried out with a generalized inverse matrix using singular value decomposition and solving for velocity (e.g. Berardino *et al.* 2002), rather than displacement, to avoid

Q6

Table 1. Selected literature examples of the identification and/or mitigation of water vapour signals over volcanoes

Volcano	Maximum magnitude of atmospheric delay (cm)	Volcano height (m)	Explicit means of identification as stratified water vapour	Mitigation method	Reference
Mount Cameroon	11	4095	Phase–elevation correlation and seasonal correlation with MODIS and GPS water vapour measurements	–	Helono <i>et al.</i> (2010)
Sakura jima	8	1117	Phase–elevation correlation	Network adjustment based on phase–elevation relationship	Remy <i>et al.</i> (2003)
Soufrière Hills	6	915	Implicit in correction	GPS water vapour correction	Wadge <i>et al.</i> (2006)
Popocatepetl	7	5426	Comparison to predicted delay from meteorological model	Correction of un wrapped phase with model delay	Pinel <i>et al.</i> (2011)
Colima	17	3850	Comparison to predicted delay from meteorological model	Correction of un wrapped phase with modelled delay	Pinel <i>et al.</i> (2011)
Etna	c. 6	3330	Comparison with atmospheric model	Correction from high-resolution atmospheric model	Wadge <i>et al.</i> (2002, 2010)
Hualca Hualca	4	5967	Pair-wise logic, time independence	–	Pritchard & Simons (2004)

291
292
293
294
295
296
297
298
299
300
301
302
303
304
305
306
307
308
309
310
311
312
313
314
315
316
317
318
319
320
321
322
323
324
325
326
327
328
329
330
331
332
333
334
335
336
337
338
339
340
341
342
343
344
345
346
347
348

349
350
351
352
353
354
355
356
357
358
359
360
361
362
363
364
365
366
367
368
369
370
371
372
373
374
375
376
377
378
379
380
381
382
383
384
385
386
387
388
389
390
391
392
393
394
395
396
397
398
399
400
401
402
403
404
405
406

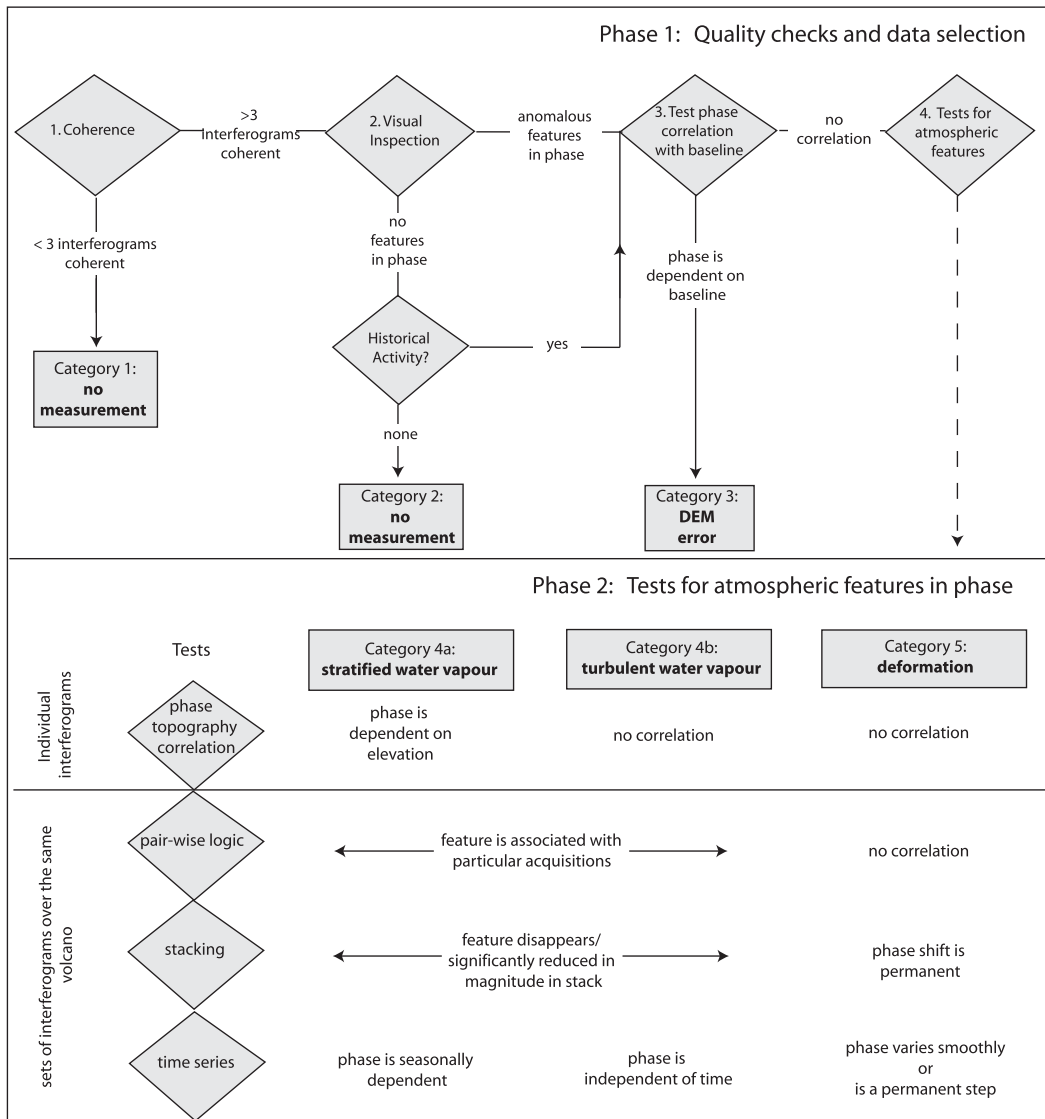


Fig. 3. Flowchart illustrating the process of analysing InSAR phase delays to: (a) Phase 1 – check the data for quality; and (b) Phase 2 – distinguish between atmospheric and deformation features.

unrealistic discontinuities. This problem is commonly rank deficient where there are subsets of interferograms that do not hold an acquisition in common. We therefore solve for velocity relative to the first date, which we explicitly define as showing no deformation.

We find the root mean squared (r.m.s.) variation of the time series after the removal of any linear trend. The r.m.s. variation of the remaining signal is used as an indicator of the average magnitude of atmospheric delay at each volcano, and will not be affected by steady deformation signals at any

volcanoes that are deforming (e.g. Arenal). The residual appears random with no systematic seasonal or similar trend. Root mean squared variation shows a linear relationship with the difference in topographical height between the edifice and the mean height of the reference annulus (Fig. 6). Excluding one outlier (Santa Ana, El Salvador) the time series r.m.s. variation increases with height difference between the edifice and reference annulus with a best-fit gradient of 2 cm/km height difference (Fig. 6). The high value at Santa Ana is thought to be associated with an unusually large

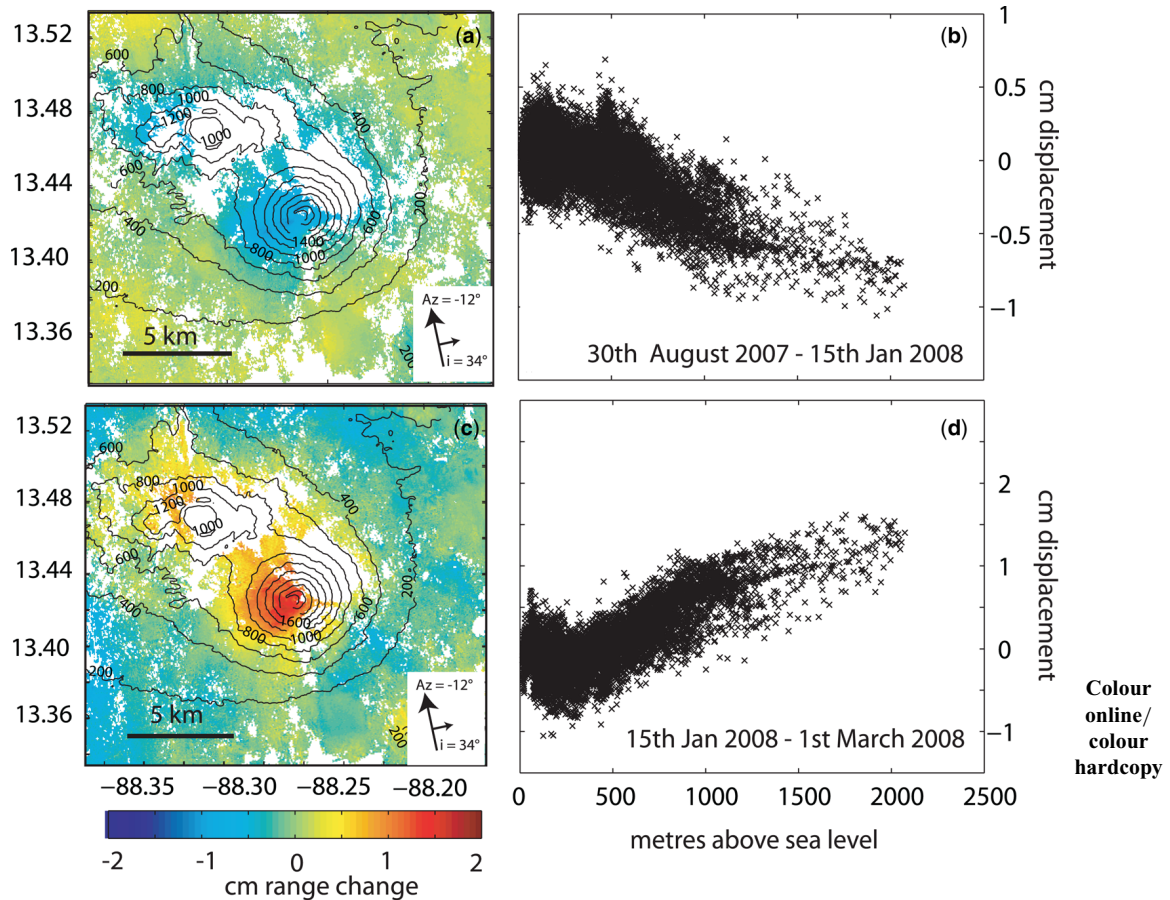


Fig. 4. Two interferograms (a & c) of San Miguel, El Salvador sharing a common date and their associated plots of range change against topographical height (b & d) on the edifice.

topographically correlated phase in one interferogram (Track 171, 9 March–9 September 2009) and the removal of this interferogram from the time series reduces r.m.s. variation at Santa Ana to 3.8 cm, well within the normal distribution. There are no similar features in other interferograms for Santa Ana, and the time series is otherwise very similar to that for nearby cinder cone Izalco (just under 5 km south of Santa Ana).

This relationship between volcano edifice height and magnitude of atmospheric phase artefact has implications for the uncertainties of InSAR measurements at different volcanoes. For transient deformation (taking place over a period greater than the satellite repeat time) to be distinguishable from normal atmospheric variation at a volcano of edifice height exceeding 2000 m (e.g. Fuego), it must exceed about 4 cm, while we may be able to detect much lower magnitude deformation (>1 cm) at low-relief volcanoes (e.g. Masaya). Although not

possible with this dataset, if the interferograms were limited to those from the same season (e.g. winter–winter or summer–summer), we hypothesize that the relationship between topographical height and atmospheric variation might be weaker.

Potential for mitigation of atmospheric effects

Several methods have been proposed (such as stacking, empirical corrections, external data and models) by which atmospheric artefacts can be reduced or removed (e.g. Hanssen 2001; Remy *et al.* 2003; Li *et al.* 2005, 2006; Wadge *et al.* 2006). In this subsection, we outline each method and assess its applicability to the volcanoes of Central America.

As turbulent water vapour artefacts are essentially random in time, stacking a set of

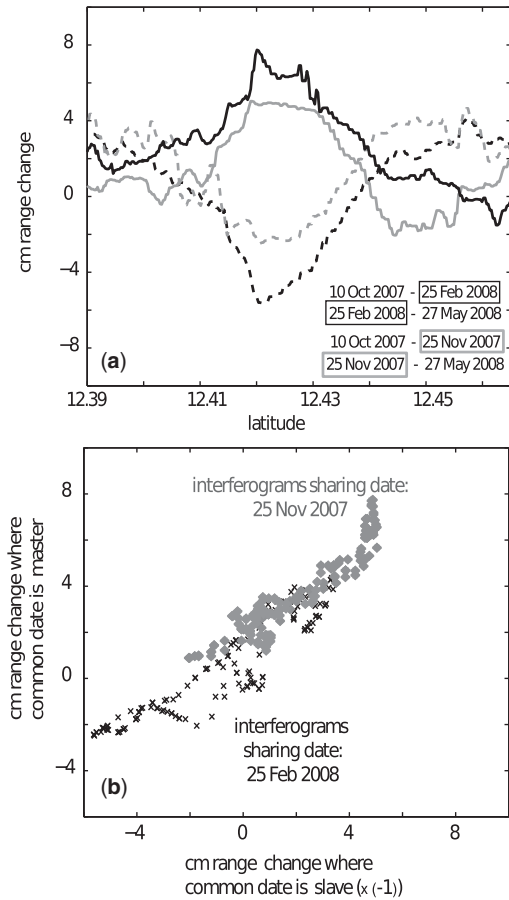


Fig. 5. (a) North–south LOS range–change transects through a pair of interferograms from Momotombo Volcano, Nicaragua. The fact that these lines are very close to being mirror images shows that the largest contribution to phase is associated with the date held in common and reflects an atmospheric artefact. Lines of the same shade hold an acquisition date in common. (b) Scatter plot of phase from the interferogram where common date is the master against (-1) phase from the interferogram where common date is slave.

interferograms together will increase the signal to noise ratio. For deformation of a constant rate, a standard stack composed of N interferograms of equal time span will increase the signal noise ratio by \sqrt{N} , whereas a chain stack (where interferograms span consecutive periods of time) will increase the signal to noise ratio by a factor of N , as the atmospheric components on each slave image will cancel with the master of the subsequent image (Biggs *et al.* 2007). However, the improvement in signal to noise ratio is achieved at a loss of temporal resolution, and is therefore better suited to studying

long-term rather than transient volcano deformation events.

Empirical corrections for stratified water vapour can be made on the basis of correlations between phase and topography. This is most robust for very large datasets with high temporal repeatability, so that analysis of phase–topography correlations for a set of interferograms can be used to make adjustments to the network of interferograms (e.g. Beauducel *et al.* 2000; Remy *et al.* 2003). Alternatively, where the area of deformation is already well constrained by other data sources, topographically correlated fringes can also be removed from individual interferograms by solving for a best-fit relationship with topography, sometimes treated as linear (e.g. Wicks *et al.* 2002), but shown to be better approximated by a non-linear model for steep volcanoes (Remy *et al.* 2003). Recent studies have used band-pass decomposition (Lin *et al.* 2010) and wavelet analysis (Shirzaei & Bürgmann 2012) to find the relationships between topography and phase for different components of an interferogram.

Other approaches applied to correcting the effects of water vapour phase delays over volcanoes require direct measurements of water vapour, ideally coincident with SAR acquisitions. These include GPS measurements of water vapour (Wadge *et al.* 2002, 2006) or satellite-based measurements (e.g. MODIS: Li *et al.* 2005; Pavez *et al.* 2006). Calculation of phase delay directly from empirical water vapour and hydrostatic pressure values requires a high spatial density (limited for ground-based instruments) and high temporal density (limited for satellite instruments) of measurements in order to provide a useful correction. A low density of measurements creates particular difficulties where the water vapour field is highly dynamic, as is the case in the tropics. High-resolution weather models have been used successfully to correct for atmospheric water vapour at Etna and over Hawaii (Webley 2004; Foster *et al.* 2006; Wadge *et al.* 2006) but, so far, have only been applied over limited areas, where local atmospheric physics is well understood.

In the absence of high densities of ground-based atmospheric measurements for calibration and an understanding of the dynamic weather systems around individual volcanoes, regional InSAR surveys of volcano deformation such as this are generally unsuitable for correction of atmospheric artefacts. Meteorological reanalysis data (e.g. Fourrier *et al.* 2011; Jolivet *et al.* 2011) has been used to remove atmospheric contributions on a regional scale, but the low spatial resolution of weather data available makes this approach more suitable for retrieving longer wavelength interseismic deformation than the deformation of volcanoes. Empirical

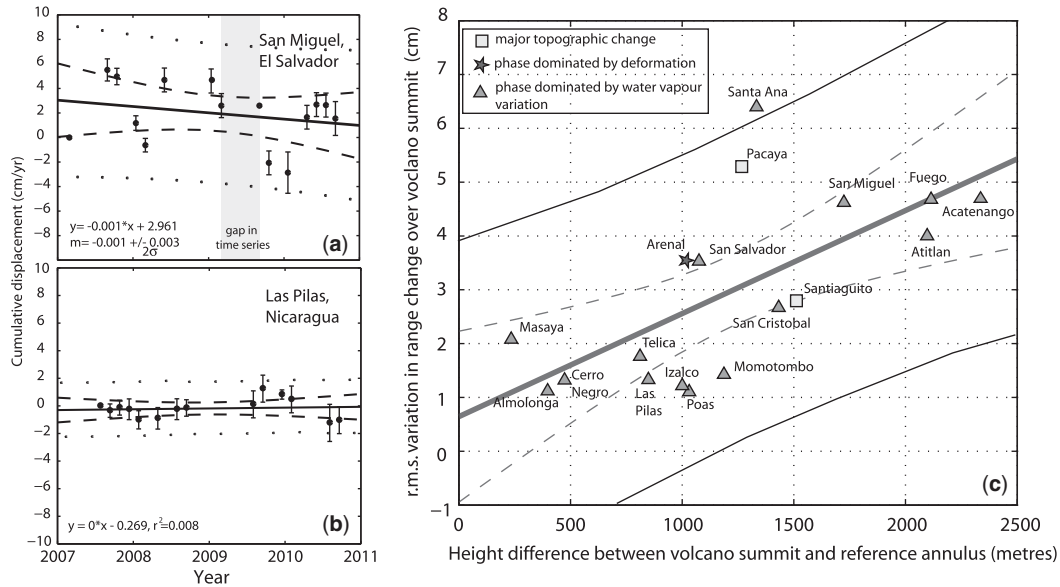


Fig. 6. (a) Time series of phase over the edifice of San Miguel, El Salvador (summit 2130 m a.s.l.) and (b) Las Pilas, Nicaragua (1088 m a.s.l.). Error bars show the standard deviation of 100 Monte Carlo repetitions of the inversion with randomly generated, non-spatially correlated noise of amplitude 1 cm added to each interferogram. (c) Plot of the r.m.s. variation in detrended time series for active volcanoes (Fig. 1) as a function of the height different between volcano summit area and the average topographical height of the reference annulus. The thick solid line shows the line of best-fit, the dotted line shows the 95% confidence envelope for the gradient, and the thinner solid line in (c) and dots in (a) and (b) show the 95% confidence envelope for any individual point.

atmospheric corrections from an assumed relationship with topography are particularly likely to introduce artefacts or to remove elements of any masked deformation signal. They are most appropriate where the nature of the expected deformation signal is known from other sources. Therefore, we did not attempt to remove water vapour variations from any of the Central American data.

Limitations of global DEMs and mitigation

Digital elevation models are used to correct for the change in path length associated with the satellite position between acquisitions. Errors or gaps in the DEM propagate into the interferogram, creating phase shifts ($\Delta\phi_{\text{topo}}$), which are proportional to the satellite perpendicular baseline (B_{perp}), and inversely proportional to radar wavelength (λ), incidence angle (θ_i) and range of satellite from the ground (r) (e.g. Rodriguez & Martin 1992; Zebker & Villasenor 1992):

$$\delta\phi_{\text{topo}} = \frac{4\pi B_{\text{perp}}}{r\lambda \sin \theta_i} \delta z. \quad (3)$$

Such topographical phase changes can be identified by examining the relationship between phase

($\Delta\Phi$) and perpendicular baseline (B_{perp}) for a set of interferograms, and can be the result of a change in topography since the DEM data were acquired (e.g. fresh lava flows emplaced since the DEM's acquisition: Ebmeier *et al.* 2012) or an error in the DEM itself (Fig. 7b, c). For the same perpendicular baselines, topographical artefacts would be greater for C-band than L-band data but, in practice, the baselines for ALOS are generally much larger than for Envisat, and will produce greater topographical errors.

Over much of the world the only DEMs available for InSAR processing are global datasets derived from satellite data, such as NASA's Shuttle Radar Topography Mission (SRTM) 90 m DEM and the Advanced Spaceborne Thermal Emission and Reflection Radiometer (ASTER GDEM). The SRTM DEM (Rosen *et al.* 2001) was acquired from a single-pass InSAR instrument on an 11 day shuttle mission in February 2000. Errors in height from SRTM data are made up of uniformly distributed, small systematic errors due to shuttle motion (>2 m) and spatially variable medium to short wavelength errors, particularly over steep topography (2–10 m) (Rodriguez *et al.* 2006). These errors are larger and more common both at lower latitudes, where fewer data were collected, and over high topographical relief, where geometric

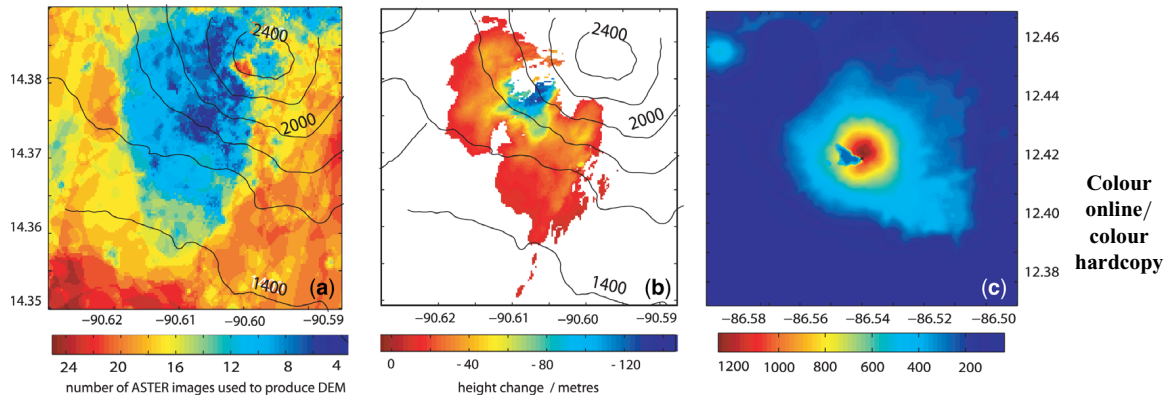


Fig. 7. (a) The number of ASTER images used to determine topographical height over Pacaya Volcano, Guatemala for each pixel. Data are not used when the ground is obscured by cloud or by the volcanic plume. (b) Map of DEM error calculated from topographical phase changes in a set of interferograms corrected using the ASTER GDEM. (c) Data gap near the summit of Momotombo, Nicaragua, SRTM 90 DEM. Similar features are found in both the SRTM and GDEM. Interpolation of such gaps generally do not result in DEM errors in interferograms.

decorrelation in phase (see the ‘InSAR’ subsection earlier in this paper) has most impact (Rodriguez *et al.* 2006). The volcanic arc in Central America falls into both of these categories, and can be expected to have errors of the order of 10 m, which correspond to path length artefacts of magnitude 0.5–2 cm for ALOS interferograms (typical baselines 500–2000 m).

The ASTER GDEM (Reuter *et al.* 2009) was constructed from Aster band-3 near-infrared imagery. DEMs are produced from the 10 year archive of stereo-pairs of ASTER images, cloud-covered areas are masked out and the DEMs are stacked; the final ASTER GDEM records the best-fit topography for the non-cloudy images. The average r.m.s. error in GDEM heights is 18–29 m (Reuter *et al.* 2009). The largest uncertainties are expected to be in areas of frequent cloud cover where the DEM was constructed from small numbers of ASTER stereo-pairs (e.g. Pacaya: Fig. 7a, b).

For the Central American ALOS data, we used the SRTM DEM, interpolated to a resolution of 30 m. For a few volcanoes where there were issues with the SRTM data or where we expected significant topographical change since 2000, we also compared our results to interferograms corrected using ASTER GDEM. Despite gaps in the SRTM DEM around some volcano summits (e.g. Momotombo, Nicaragua: Fig. 7c), the interpolated version was accurate enough to allow us to process interferograms without introducing artefacts into the phase. However, the GDEM was found to introduce artefacts, presumably owing to the low number of cloud-free images (Ebmeier *et al.* 2012). With enough interferograms and a large enough range of baselines, it may be possible to use

Equation (3) to calculate errors in topographical height with an accuracy sufficient to correct any errors in the DEMs, although this may be limited by poor phase coherence around summit areas where most DEM errors occur.

Both SRTM and GDEM have very low spatial resolutions (90 and 30 m, respectively) compared with new X-band SAR data (3 m), such as that from TerraSAR-X (TSX). These new data will be most useful over small areas where deformation is known to be taking place and a high-resolution local DEM can be acquired.

Geometric distortion and optimal acquisition strategy

Radar satellites produce images in range and azimuth co-ordinate systems, which, owing to the effects of topography, may be distorted in comparison with ground-based co-ordinate systems (e.g. Fig. 8a–d). Interferograms are reprojected into latitude and longitude (geocoded) using a DEM (e.g. Fig. 8c, d). The extent of the geometric distortions depends on the radar look angle and the steepness of topography, and can cause problems for measurements at steep-sided stratovolcanoes (e.g. Atitlan, Guatemala).

Where the slope is steep, but the angle is less than the satellite look angle, the side of a volcano facing the satellite becomes foreshortened – the geocoded pixel size is smaller on the far side of volcano than the near side. For slope angles exceeding the satellite look angle, returns from the top of the slope will arrive before those at the bottom (layover: Fig. 8e) and parts of the far side of the

Colour
online/
colour
hardcopy

639
640
641
642
643
644
645
646
647
648
649
650
651
652
653
654
655
656
657
658
659
660
661
662
663
664
665
666
667
668
669
670
671
672
673
674
675
676
677
678
679
680
681
682
683
684
685
686
687
688
689
690
691
692
693
694
695
696

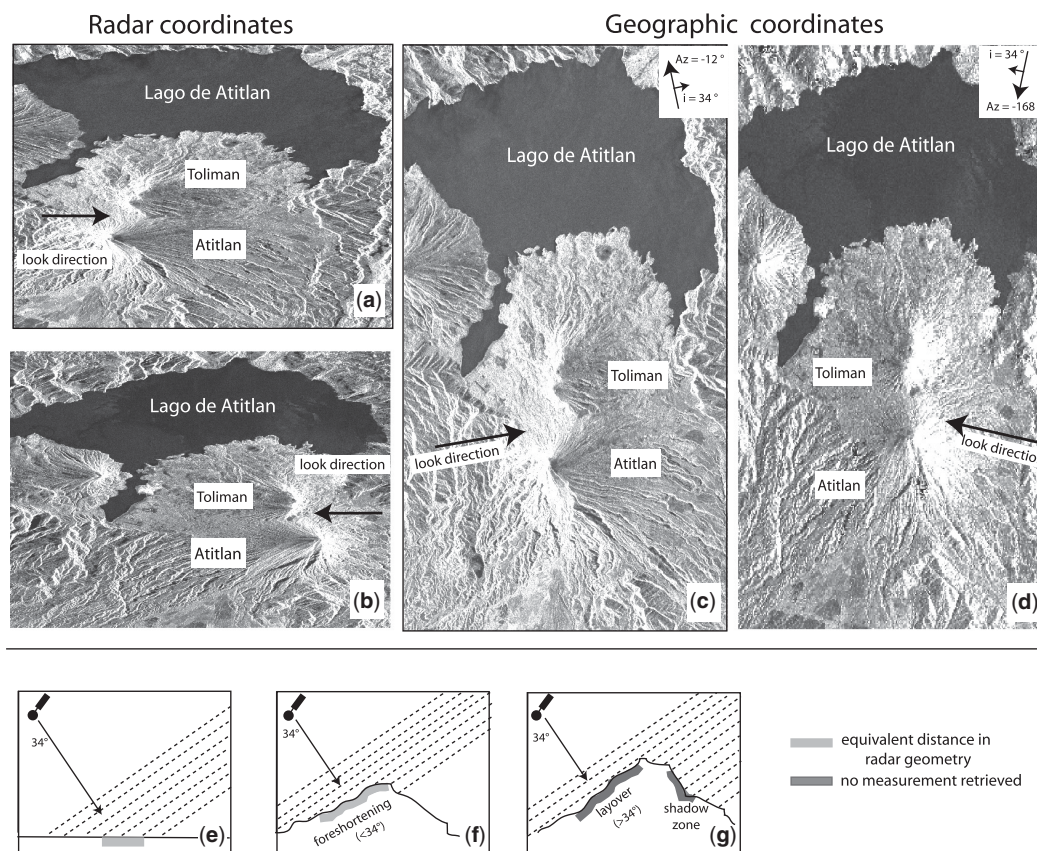


Fig. 8. (a) Example of an amplitude image of the Atitlan and Toliman volcanoes in ascending radar geometry (b) Amplitude image of Atitlan and Toliman in descending radar geometry. (c) Ascending amplitude image reprojected into latitude and longitude showing foreshortening of the western slope. (d) Descending amplitude image in latitude and longitude showing foreshortening of the eastern slope. (e)–(g) Cartoons showing the conditions that lead to foreshortening, layover and shadow, when volcano slopes exceed the satellite look angle. The satellite is moving into the page in each instance, the arrow shows the satellite line of sight and the dotted lines indicate points of apparently equal distance from the satellite.

volcano will not produce a radar return (shadowing). At some of the steepest volcano summits in Central America we observe a layover and shadow effects (e.g. Fuego or Atitlan, Guatemala). In this case there can be no correction and data for that section of the volcano cannot be used. Foreshortening and layover will also have an effect on coherence as the radar potentially samples a much greater area of the ground, effectively increasing the pixel ‘size’ (see Fig. 8f).

To ensure that there is good resolution on all parts of steep volcanic edifices, it is necessary to have images from both ascending and descending paths. Many deformation signals are isolated to only one part of a volcanic edifice. For example, Fournier *et al.* (2010)’s analysis of ascending data over a large proportion of Latin America did not

show up asymmetrical gravity-driven deformation at Arenal, Costa Rica (Ebmeier *et al.* 2010), which is only clearly observable in descending interferograms. Furthermore, since InSAR only measures displacement along the satellite line of sight, any motion perpendicular to this vector will not be detected and images from both look directions are required to determine the direction of the vector displacement.

In Central America, the majority of acquisitions made were on ascending passes due to JAXA’s acquisition strategy but, for this study, we were able to produce at least one descending interferogram over almost all currently active volcanoes (see Fig. 1a, b). For steep-sided volcanoes, acquisition strategies incorporating both ascending and descending tracks are particularly advantageous.

697 **Coherence in Central America**

698
699 The poor radar penetration of dense tropical veg-
700 etation using widely used SAR instruments (e.g.
701 ERS, ASAR and ENVISAT) has been the primary
702 factor limiting InSAR measurements in many parts
703 of the tropics. The effect of vegetation on InSAR
704 is dependent on wavelength, with L-band radar
705 ($\lambda = 23$ cm) maintaining coherence much better
706 than C-band radar ($\lambda = 5.6$ cm). The relative coher-
707 ence between two interferograms showing the
708 same part of the ground will depend on numerous
709 factors in addition to SAR wavelength, including
710 time spanned, perpendicular baseline, differences
711 between surface scatterers and different rates of
712 instrument-related decorrelation (e.g. Zebker & Vil-
713 lasenor 1992; Hanssen 2001). As interferometric
714 correlation (γ) is estimated from phase values for
715 a set of neighbouring pixels (Equation 2), pixel
716 dimensions are also important. In addition, choices
717 made during InSAR processing, such as spatial
718 wavelength of filtering and degree of multilooking
719 (reduction of spatial resolution with the aim of
720 increasing the size of a coherent area), will also
721 affect our estimations of correlation. Owing to the
722 nature of the estimator used to examine interfero-
723 metric correlation (Equation 2), areas that are
724 entirely incoherent will still produce an apparent
725 coherence value. We therefore use empirically
726 derived ‘threshold’ coherence when comparing the
727 coherence of interferograms processed to different
728 number of looks (multilooking consists of taking a
729 weighted average of neighbouring complex pixels:
730 the greater the number of looks, the lower the
731 spatial resolution) in the subsection ‘SAR wave-
732 length comparison: Arenal, Costa Rica’ later.

733 We use the data from our arc-scale survey, out-
734 lined in Figure 1, to examine patterns of interfero-
735 metric coherence in Central America. As this is all
736 L-band ALOS data, processed in the same manner,
737 comparison between coherence as a function of
738 time and spatial baseline for different areas can be
739 made directly. Of the 26 active volcanoes in the
740 arc, L-band data for just three (Concepción, Irazu
741 and Turrialba) were too incoherent to make any
742 measurement of deformation at all. Measurements
743 are restricted at other volcanoes, however, by high
744 rates of decorrelation, which meant that only short
745 temporal baseline interferograms could be con-
746 structed. Making the distinction between water
747 vapour signals and deformation often requires
748 enough interferograms to examine the temporal
749 development of the phase, so this hampers our
750 analysis. It also imposes spatial limitations on our
751 measurements. At Arenal (see the ‘SAR wavelength
752 comparison: Arenal, Costa Rica’ subsection), for
753 example, coherence is limited to the stable surfaces
754 of young lava flows (Ebmeier *et al.* 2010). This

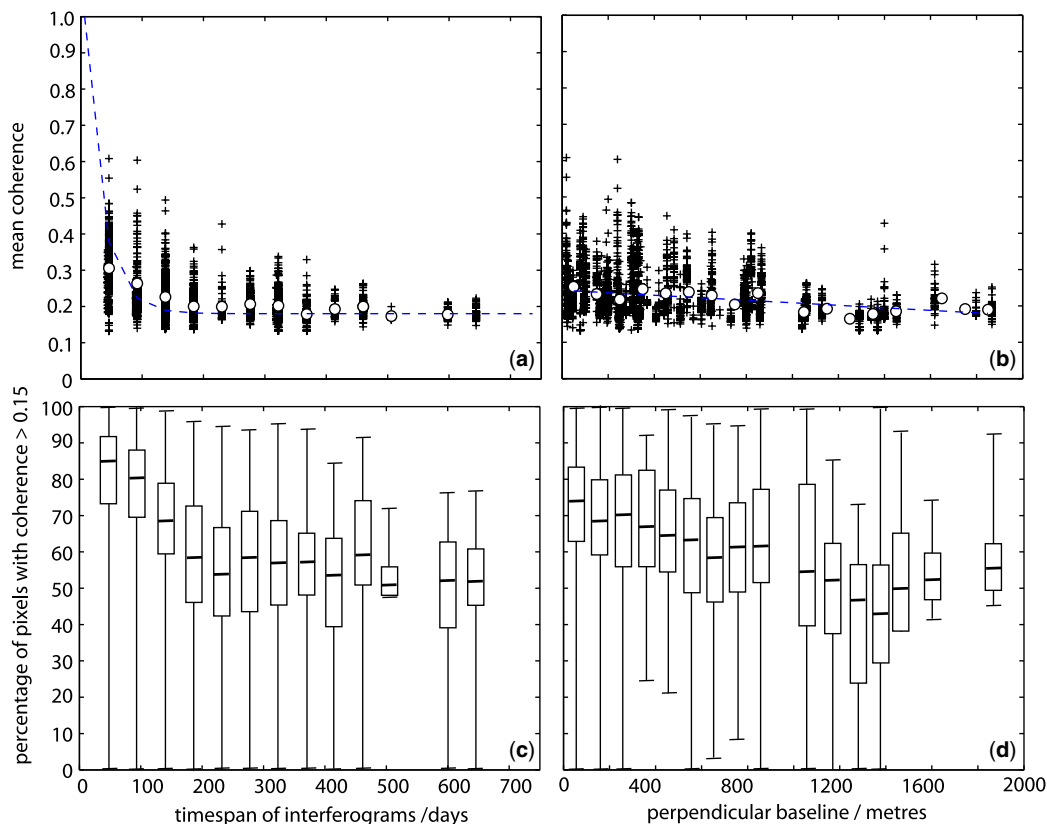
confined our measurement to a 2.5 km² region on
the western side of the volcano, making the mea-
surement of any longer wavelength deformation
impossible. The summits of volcanoes with contin-
uous or semi-continuous explosive activity, such as
Santiaguito, Fuego, Pacaya (Guatemala) or Arenal
(Costa Rica), were also consistently incoherent.

We investigate the relative importance of the
contributions of geometrical and temporal decor-
relation to patterns of coherence across Central
America. Unlike the many analytical models for
coherence used to measure (e.g. stem volume or
tree heights: see, e.g., Balzter 2001; Santoro *et al.*
2002), we do not aim to extract information about
ecological processes from InSAR coherence but to
predict where InSAR measurements at volcanoes
are likely to be useful and where they are most
likely to be limited by rapid decorrelation. Tempo-
ral decorrelation is generally caused by volcanic
activity, slope instability or, sometimes, very rapid
changes in vegetation cover (e.g. rapidly develop-
ing kill zones at Poás and Turrialba: Martini *et al.*
2010) close to a volcano’s summit. The lower
flanks of volcanoes in Central America, however,
are commonly either covered by rainforest or are
intensively cultivated. It is on the lower slopes and
surrounding area that we expect to observe any
deformation associated with deeper magmatic pro-
cesses, so understanding the relationship between
vegetation cover and decorrelation is useful for
understanding limitations on volcano deformation
measurement.

Coherence model

The mean coherence for the complete Central
American ALOS data (Fig. 9: data sampled into
0.1° × 0.1° boxes) shows a dependence on both
time span of interferogram and perpendicular base-
line. After about 200 days, mean coherence has
decayed exponentially to a value of about 0.18
compared to a value of 0.3 for interferograms
covering the shortest possible time span (46 days).
The difference between coherence in the lowest
and highest baseline interval is less significant,
falling from 0.26 to 0.19.

Mean coherence is not particularly useful as an
indicator of whether volcanic edifices will be coher-
ent as they make up a relatively small proportion
of a scene by area, and are commonly not representa-
tive of the rest of an interferogram. Fresh, young
lavas, for example, decorrelate slowly, whereas
scattering properties of explosive products alter
rapidly, especially when deposited on steep slopes.
It is considered possible to use interferometric
data where its coherence is above about 0.15, the
value used as the threshold for unwrapping routines
(e.g. branchcut algorithm: Goldstein *et al.* 1988).



Colour
online/
mono
hardcopy

Fig. 9. Mean coherence for the whole Central American dataset plotted as a function of (a) time in days and (b) perpendicular baseline. Each point represents the mean value of coherence for a $0.1^\circ \times 0.1^\circ$ box in an interferogram. The choice of resolution captures regional-scale differences in vegetation and land use. Mean values are marked with circles on (a) and (b). (c) & (d) show box and whisker plots of the percentage of pixels with correlation above 0.15 as a function of time and perpendicular baseline, respectively. The limits of the boxes are the 25th and 75th percentile, while the central black line shows the position of the median. Minimum and maximum values are shown by the extent of the black line.

The percentage of pixels above this threshold coherence and the mean coherence are related, but not directly proportional, as coherences are not normally distributed about the mean value (Fig. 9c, d). The relationships between percentage coherence above 0.15 and time or baseline are therefore not as clear as for mean coherence, but more likely to yield information useful for our purpose of investigating volcano deformation.

We model percentage coherence above 0.15 (C) as the product of exponential decay functions describing coherence in terms of time in years (t), perpendicular baseline separation (B_{perp}) and a parameter describing seasonal dependence (α). For simplicity, we neglect the effects of some instrument-dependent parameters also associated with decorrelation (rotation of satellite look angle and thermal decorrelation, as discussed by Zebker & Villasenor 1992; Hanssen 2001) that we expect

to be smaller than the contributions of geometric and temporal decorrelation. Our choice of exponential decay functions to describe temporal and geometric decorrelation is informed by analytical expressions (e.g. temporal decorrelation: Zebker & Villasenor 1992), and examination of the coherence–temporal baseline relationship and coherence–spatial baseline relationship for our complete dataset (Fig. 9):

$$C = 1 + \frac{1}{\alpha} \left(e^{-\frac{B_{\text{perp}}}{\beta}} e^{-\frac{t}{\tau}} \cos(2\pi t) - 1 \right). \quad (4)$$

The parameters β and τ reflect the dependence of coherence on B_{perp} and time spanned by the interferogram, respectively. We use non-linear inversion, where the difference between model predicted values and our coherence data were minimized using a least-squares method, to find the values of β , τ

and α that best fit the data. We checked that our results for these parameters were global, rather than local, solutions by varying the starting values for each parameter used in the least-squares method and confirming that our solutions were not affected.

The parameter α is added to the expression to allow for a seasonal difference in coherence and controls the amplitude of a cosine function with the period of a year, which moderates the shape of the exponential expressions (Fig. 10a, b). This additional parameter was found to significantly improve the fit of our model to the coherence data (e.g. reducing the residual in fit by about 20% in northern Nicaragua, Track 166). A low α value indicates that coherence has a strong seasonal dependence.

Two examples, expressed as a function of time, are shown in Figure 10a, b. The best-fit solution for Track 172 (Fig. 10a), in central Guatemala, shows slower decorrelation as a function of time and a lesser seasonal dependence than data from Track 166 (Fig. 10b) in northern Nicaragua ($\tau = 150$ and $\alpha = 4.9$, relative to 90 and 2.3). Predicted coherence above the threshold value is calculated from our best-fit values for τ , β and α for

$0.1^\circ \times 0.1^\circ$ boxes across Central America, and is shown plotted against actual coherence in Figure 10c. The spatial distribution of the r.m.s. misfit between predicted and measured percentage of pixels above threshold coherence is shown in Figure 10d.

The distribution of values of τ , β and α across Central America is spatially noisy (Fig. 11b–d) but the temporal-dependence parameters (τ and α) show some trends, which are discussed in the next subsection. β , however, takes very high values across the majority of Central America ($>10\,000$), showing that geometric factors are largely of lesser significance than time-dependent processes. The remaining lower values of β are, typically, of the order of $1000\text{--}3000\text{ m}^{-1}$, show no correlation with topographical height and are mostly isolated to two tracks with some particularly large baseline interferograms (tracks 165 and 162).

Coherence and land use

Our arc-scale analysis of coherence data shows that time-dependent processes, most probably associated with vegetation growth, dominate decorrelation

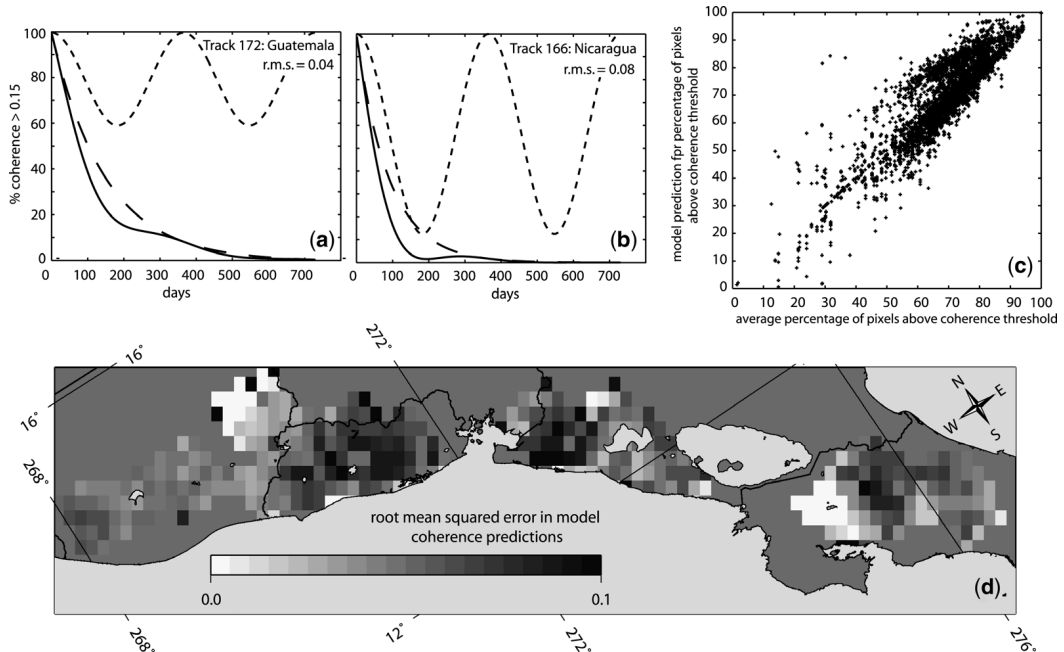
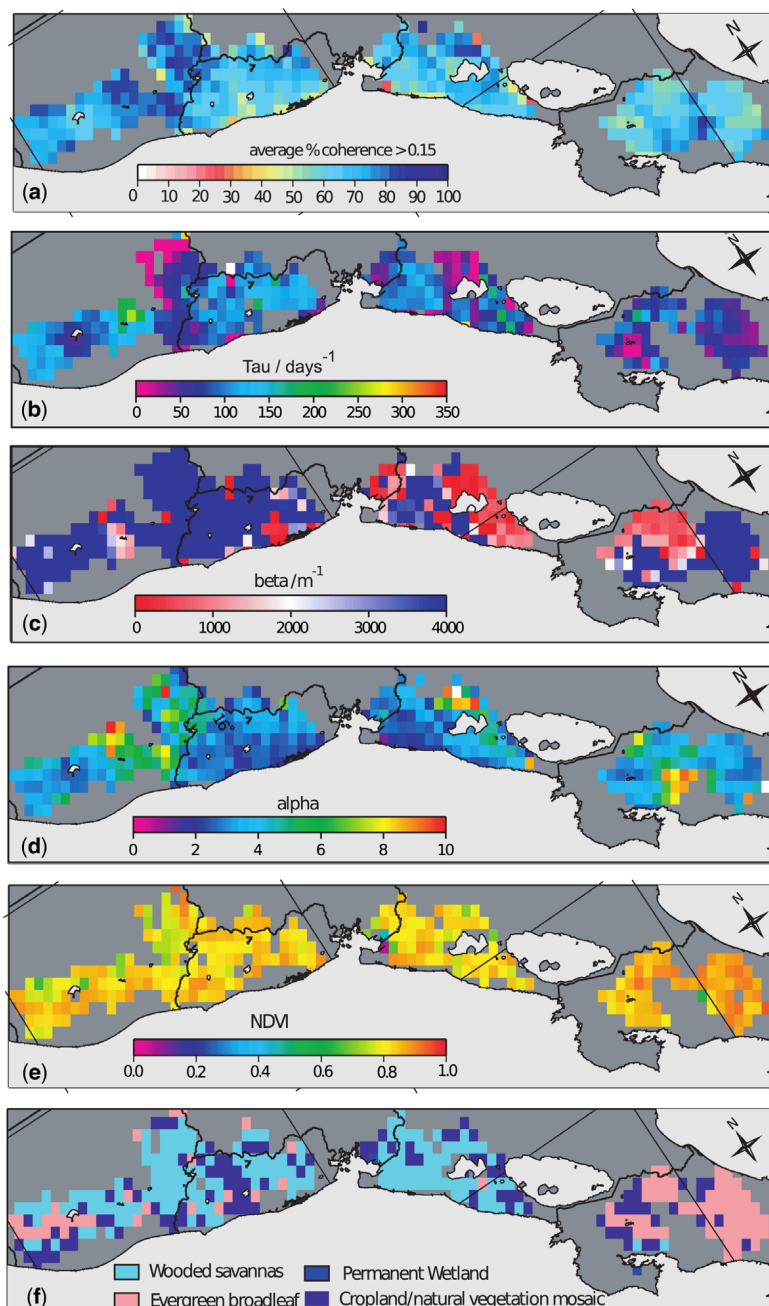


Fig. 10. Schematic examples of our simple coherence model for average coherence across (a) Track 172 in Guatemala and (b) Track 166 in Nicaragua (as shown in Fig. 1a). These show model predictions as a function of time only for percentage coherence above a threshold value of 0.15. Black dashed lines show exponential time dependence, finer dashed line shows our approximation of seasonal dependence and solid lines show the combined model. (c) Plot illustrating the fit between average percentage coherence above 0.15 for all our data at a resolution of 0.1° and model predictions for the same value. (d) Map of r.m.s. error in model predictions across Central America, using the same resolution as for Figure 11.

871
872
873
874
875
876
877
878
879
880
881
882
883
884
885
886
887
888
889
890
891
892
893
894
895
896
897
898
899
900
901
902
903
904
905
906
907
908
909
910
911
912
913
914
915
916
917
918
919
920
921
922
923
924
925
926
927
928



Colour
online/
colour
hardcopy

Fig. 11. (a) Map of mean percentage of pixels with correlation above 0.15 per box. This figure simply shows the mean values for our input dataset and makes no distinction for temporal or spatial baseline. (b) Map of Central America showing parameter τ , describing relative rate of decorrelation as a function of time (lower values indicate faster decorrelation). (c) Parameter β , describing the relative rate of decorrelation as a function of baseline. Where the colour scale is saturated, β values are very high (exceeding 10 000), indicating that coherence is not strongly dependent on baseline. (d) Parameter α describes the strength of any seasonal dependence of decorrelation (lower values indicate greater seasonal effect). (e) NDVI from MODIS level 3 'atmosphere' product at 1° resolution, resampled to the same resolution as our calculations of τ . (f) Land-use map from MODIS level 3 'land' product, resampled to 0.1° × 0.1° resolution. Land use is classified according to the International Geosphere–Biosphere Programme (IGBP) index.

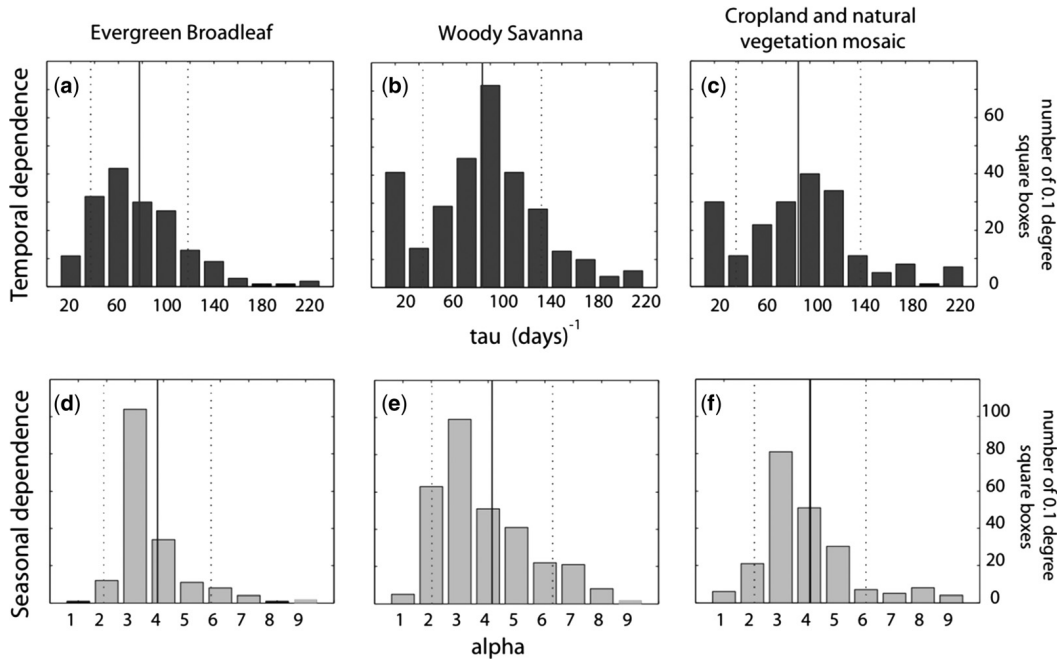


Fig. 12. Histograms showing distribution of values for IGBP classifications (a) ‘Evergreen broadleaf’, (b) ‘Woody savanna’ and (c) ‘Cropland/natural vegetation mosaic’ environments. (d), (e) & (f) show distributions of α . Dotted lines show the mean value.

rates (e.g. Fransson *et al.* 2001; Liu *et al.* 2001). We might, therefore, expect the Normalized Difference Vegetation Index (NDVI) to be a useful predictor for interferometric coherence. Correlations between NDVI and coherence have been observed in data from other parts of the world (e.g. Hawaii: Rosen *et al.* 1996; NW China, Liu *et al.* 2010), with higher NDVI values being associated with poor coherence. In Central America, however, there is no systematic relationship between NDVI and either τ or α (Fig. 12b, d, e). NDVI varies very little across Central America (although it takes slightly higher values in Costa Rica than further north) because vegetation index is similar for both rainforest and cultivated land. Comparison of NDVI with a MODIS land-cover map using International Geosphere–Biosphere Programme (IGBP) classifications shows no clear relationship between type of land cover and NDVI (Fig. 11e, f).

The temporal parameter τ and, to some extent, our seasonal parameter α show distinct distributions for areas of different IGBP land-use classification (Fig. 12). For ‘Evergreen broadleaf,’ dominated by tropical rainforest and cloud forests in Central America, τ has a left-skewed distribution with a mode interval of 50–70 day^{-1} (Fig. 12a). The less densely vegetated land, ‘Cropland/vegetation’ and ‘Woody savanna’, decorrelate less quickly (modes

of 90–110 day^{-1} : Fig. 12b, c). These classifications are likely to include more developed landscapes, including agricultural areas where surface scatterers are regularly altered due to human activity (e.g. ploughing, harvesting). We attribute the high number of pixels showing very low values for τ in these categories to be caused by human interference with the landscape.

Our parameter describing the seasonal dependence of coherence, α , takes an average value of 2.5 across all land-cover classifications, suggesting some seasonal trends in coherence across the whole area of study (Fig. 12d–f). The distribution in values is slightly more left-skewed in the ‘Evergreen broadleaf’ land-cover category than where vegetation was less dense, a feature we attribute to seasonal agricultural practices increasing the numbers of low values for α . Seasonal effects are smallest over high topography in Guatemala, Costa Rica and NW of Lake Managua in Nicaragua, and largest in the coastal regions of El Salvador and Nicaragua. We see a very small range of values for α in areas dominated by rainforest (‘Evergreen broadleaf’: Fig. 12d), and much greater seasonal variation where land-use category suggests some degree of cultivation (Fig. 12e, f).

We use the IGBP land-use classifications to make coarse predictions of decorrelation rate for

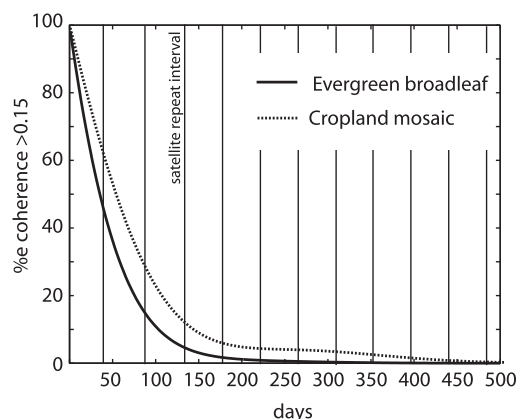


Fig. 13. Graph showing predicted decorrelation as a function of time for ‘Evergreen broadleaf’ (mostly rainforest) and ‘Cropland/natural vegetation mosaic’ land uses.

different land types. On average, we expect rainforest environments to decorrelate faster than cropland (Fig. 13), with the largest differences between the two environments in the shortest possible interferograms (46 and 92 days for ALOS). However, this simple approach will not capture the detailed spatial patterns of coherence seen in Figure 11a. The IBGP classifications ‘Cropland/vegetation mosaic’ and ‘Woody savanna’, in particular, deviate from a normal or skewed normal distribution of the temporal decorrelation parameter, τ (Fig. 12b, c). There are significant parts of Central America where these environments decorrelate much more quickly than the average, as shown by the peaks at low values for τ in Figure 12b, c.

SAR wavelength comparison: Arenal, Costa Rica

Data from four different satellite instruments (ERS, RadarSat, ALOS and TSX: see Table 2) were used to make measurements at Arenal Volcano, Costa

Rica, which is known to be deforming (Ebmeier *et al.* 2010). To make a meaningful comparison of coherence between these different platforms we use the average value for a section of the interferogram over Lake Arenal as a ‘threshold’ value for interferometric correlation. As reflected and back-scattered radiation from the lake surface will be completely incoherent, any value below this threshold shows that data are unusable. The actual value of this threshold will depend on a combination of the factors listed above (see the ‘InSAR’ and ‘Coherence model’ subsections), but the percentage of pixels above threshold coherence will show the proportion of data that may yield useful interferometric deformation measurements. The percentage of pixels above the given threshold value are shown in Figure 14, and are plotted with respect to temporal and spatial baseline in Figure 15.

Phase correlation in the area around Arenal is among the lowest in Central America, with high phase correlation exclusively over the young lava around the volcano in the majority of interferograms. As expected, owing to its longer wavelength, L-band data produce the greatest proportion of pixels over the coherence threshold, followed by the TSX interferogram, which has a smaller pixel size. All of the TSX interferograms constructed showed significantly better coherence than ERS or RadarSat interferograms of equivalent temporal length. The proportion of pixels above threshold coherence were generally slightly higher in the RadarSat than in the few ERS interferograms, and this is probably due to shorter perpendicular baselines (Fig. 15b).

Although L-band data produce the greatest proportion of coherent pixels, over extremely stable surfaces such as lava flows we find that RadarSat data maintain coherence for up to 600 days (Fig. 15a), illustrating that C-band data are useful for measuring the deformation of small, stable areas. To date, only L-band data have been demonstrated to be suitable for surveying arcs as a whole in the tropics (e.g. Philibosian & Simons 2011). High-resolution, short-repeat-time X-band InSAR data

Table 2. SAR satellite instrument parameters referred to in the text

Instrument	Period operational	Wavelength (cm)	Repeat interval (days)	Typical look angle (°)	Range resolution (m)	Azimuth resolution (m)
ERS-1/2 (ESA)	1992–2000/ 1995–2011	5.66 (C-band)	35	<i>c.</i> 23	10	5
ALOS (JAXA)	2006–2011	23.61 (L-band)	46	10–51	9–30	10
RadarSat-1/2 (CSA)	1995/2007–	5.66 (C-band)	24	20–49	25	25
TerraSAR-X (DLR)	2008–	3.12 (X-band)	11	20–45	2–3	3
SENTINEL (ESA)	2013–onwards?	5.66 (C-band)	12	20–46	5	5

INSAR FOR TROPICAL VOLCANOES

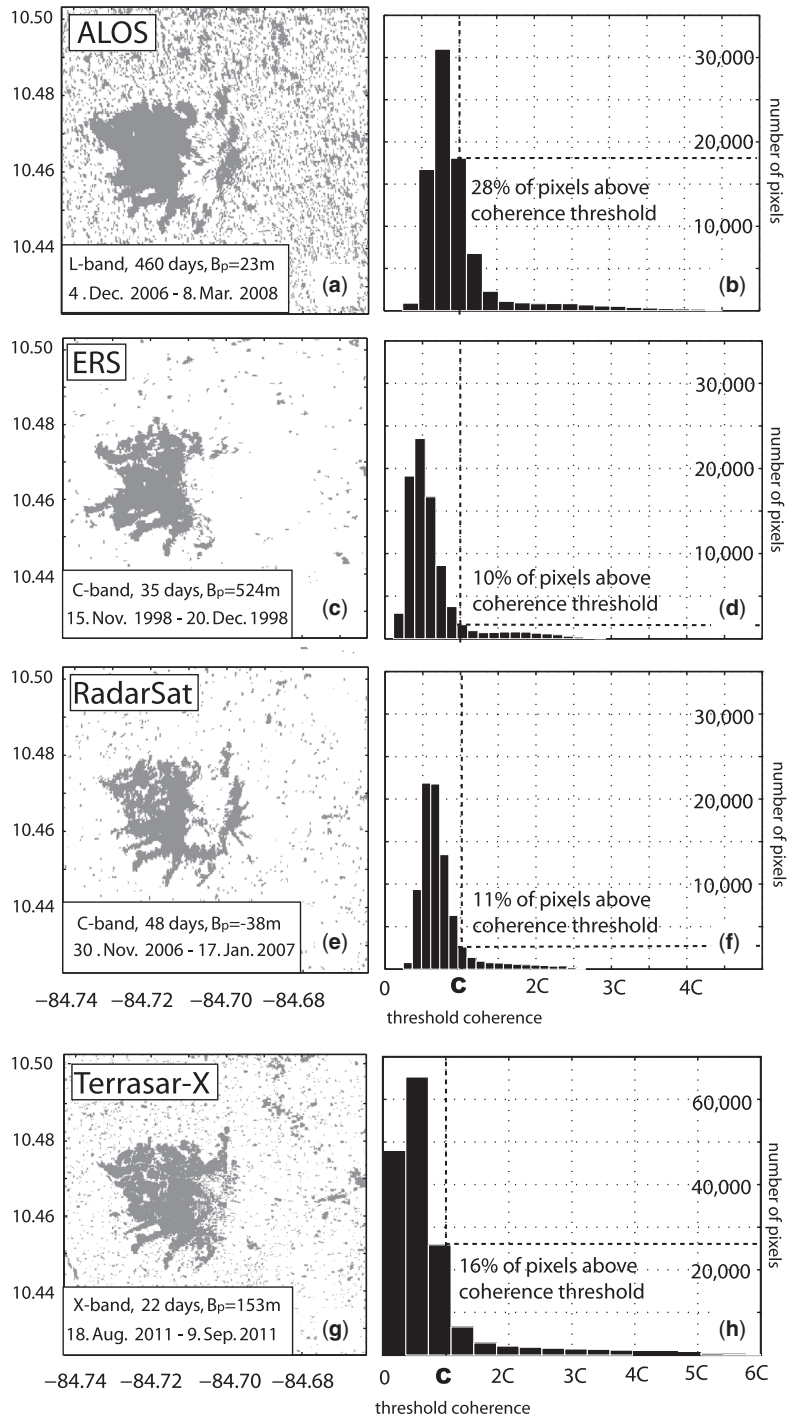


Fig. 14. Maps showing pixels above (grey) and below (white) the threshold coherence around Arenal for (a) ALOS, (c) ERS, (e) RadarSat and (g) Terrasar-X interferograms. Threshold values were found from the mean correlation value over part of Lake Arenal and were 0.18, 0.3, 0.35 and 0.1, respectively. Corresponding histograms show the distribution of pixels about this value. The boundary between data above and below the coherence threshold value is marked with a dotted line. Note the different scales on the x- and y-axes for the TSX data. The data points corresponding to each of the interferograms shown here are marked on Figure 15 by black boxes.

1045
1046
1047
1048
1049
1050
1051
1052
1053
1054
1055
1056
1057
1058
1059
1060
1061
1062
1063
1064
1065
1066
1067
1068
1069
1070
1071
1072
1073
1074
1075
1076
1077
1078
1079
1080
1081
1082
1083
1084
1085
1086
1087
1088
1089
1090
1091
1092
1093
1094
1095
1096
1097
1098
1099
1100
1101
1102

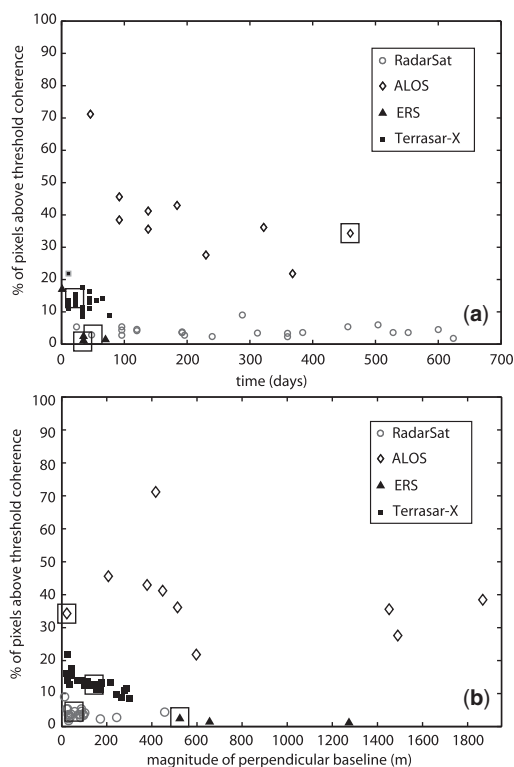


Fig. 15. Percentage of pixels above threshold coherence calculated for our complete dataset at Volcàn Arenal, Costa Rica, shown as a function of (a) time span and (b) magnitude of perpendicular baseline. The interferograms shown in Figure 14 are indicated by black boxes.

may prove useful for individual volcanoes but is currently prohibitively expensive for large-scale mapping. The upcoming European Space Agency instrument, Sentinel (Table 2), will be C-band but have a higher spatial resolution and shorter repeat time than ERS and RadarSat. We therefore expect these new data to be much more useful than earlier C-band instruments, although it seems unlikely that it will be as suitable for regional-scale surveys in the way that the ALOS L-band data are. These results agree with expectations (e.g. Rosen *et al.* 1996), but this is the first time that coherence has been quantified for such a large dataset.

Summary

Our analysis of data from Central America demonstrates factors that determine the usefulness of InSAR at volcanoes both within the tropics and worldwide. In summary, water vapour artefacts and poor coherence are the greatest challenges to making successful InSAR measurements at

volcanoes. This means that the characteristics of volcanoes worldwide that inhibit measurement of deformation with InSAR include: (1) vegetation cover that leaves little of the ground exposed (e.g. rainforest); (2) persistent activity changing surface scatterer properties; (3) steep slopes; and (4) large contrasts in topography. Thus, young stratovolcanoes present particularly difficult targets for measurement with InSAR. Recent activity can, however, present some advantages for InSAR as young lavas present more stable scattering surfaces for InSAR than older, densely vegetated slopes. Steep slopes at many volcanoes also make acquisition and analysis strategy (i.e. including both ascending and descending tracks) more important than in other geographical settings.

Two of the most important limiting factors for measuring volcano deformation with InSAR – water vapour artefacts and vegetation-related loss of coherence – are particularly significant in the tropics. Root mean squared variations in path delay due to stratified water vapour changes reached as much as 6.4, 5.3 and 4.8 cm at Santa Ana, Pacaya and Fuego, respectively (Fig. 6). For our data, this variability in path delay over a volcano is proportional to the difference between edifice height and the surrounding topography (gradient of 2 cm/km height). Although the presence of water vapour artefacts does not prevent InSAR phase measurements from being made, it may mask deformation signals, complicating interpretation at volcanoes with high relief. Furthermore, very steep slopes can lead to layover and foreshortening in the radar geometry (Fig. 8). One satellite look angle is not necessarily sufficient to be sure of detecting deformation.

In Central America, the lower slopes of most volcanoes as well as the surrounding areas are vegetated to some extent. The degree to which this affects InSAR measurement depends on the type and density of vegetation, and has implications for the measurement of deeper magmatic movement. In general, decorrelation rates are greater in the southern arc than in the north, although there is considerable variability (Fig. 11a). Although there is no relationship with NDVI, coherence shows some consistent variation with land-use type, such that decorrelation rates are higher and standard deviation lower for tropical rainforest than for cultivated land (Fig. 12).

Our comparison of L-, C- and X-band results in one of the least coherent parts of Central America demonstrates the importance of having L-band data for measuring volcano deformation in the tropics (Figs 14 & 15). The application of C-band data of varying spatial resolutions is limited to small, stable areas. X-band radar shows potential for penetrating vegetation to allow measurements

1161 over a larger spatial area, but only over short
 1162 (<100 day) time periods, and where it is possible
 1163 to obtain a high-resolution DEM. We expect Senti-
 1164 nel data to perform better than ERS or RadarSat data
 1165 due both to its shorter proposed repeat time and its
 1166 higher spatial resolution. It is unlikely, however,
 1167 to allow measurements over regions as large as for
 1168 L-band data in tropical areas.

1170 All ALOS data were acquired through the WInSAR
 1171 programme at the University of Miami from JAXA via the
 1172 Alaskan Satellite Facility. This work was supported by
 1173 the National Environmental Research Council through
 1174 the National Centre for Earth Observation (NCEO), of
 1175 which the Centre for the Observation and Modelling of
 1176 Earthquakes, Volcanoes and Tectonics (COMET+) is a
 1177 part. S. K. Ebmeier is supported by an NCEO studentship
 1178 and J. Biggs was funded by the ESA Changing Earth
 1179 Science Network and a Rosenstiel Postdoctoral Fellowship
 1180 at the University of Miami. We thank M. Shirzaei and
 1181 M. Pritchard for their helpful reviews.

1182 **References**

1183 AHMED, R., SQUEIRA, P., HENSLEY, S., CHAPMAN, B. &
 1184 BERGEN, K. 2011. A survey of temporal decorrelation
 1185 from spaceborne L-Band repeat-pass InSAR. *Remote*
 1186 *Sensing of Environment*, **115**, 2887–2896, <http://dx.doi.org/10.1016/j.rse.2010.03.017>
 1187
 1188 BALZTER, H. 2001. Forest mapping and monitoring with
 1189 interferometric synthetic aperture radar (InSAR). *Pro-*
 1190 *gress in Physical Geography*, **25**, 159–177, <http://dx.doi.org/10.1177/030913330102500201>
 1191
 1192 BEAUDUCEL, F., BRIOLE, P. & FROGER, J. 2000. Volcano-
 1193 wide fringes in ERS synthetic aperture radar interfero-
 1194 grams of Etna (1992–1998): deformation or tropo-
 1195 spheric effect? *Journal of Geophysical Research*,
 1196 **105**, 16 391–16 402, <http://dx.doi.org/10.1029/2000JB900095>
 1197
 1198 BERARDINO, P., FORNARO, G., LANARI, R. & SANSOSTI, E.
 1199 2002. A new algorithm for surface deformation moni-
 1200 toring based on small baseline differential SAR inter-
 1201 ferograms. *IEEE Transactions on Geoscience and*
 1202 *Remote Sensing*, **40**, 2375–2383, <http://dx.doi.org/10.1109/TGRS.2002.803792>
 1203
 1204 BEVIS, M., BUSINGER, S., HERRING, T. A., ROCKEN, C.,
 1205 ANTHES, R. A. & WARE, R. H. 1992. GPS meteorol-
 1206 ogy: remote sensing of atmospheric water vapor
 1207 using the Global Positioning System. *Journal of Geo-*
 1208 *physical Research*, **97**, 15 787–15 801.
 1209
 1210 BIGGS, J., WRIGHT, T., LU, Z. & PARSONS, B. 2007. Multi
 1211 interferogram method for measuring interseismic
 1212 deformation: Denali Fault, Alaska. *Geophysical*
 1213 *Journal International*, **170**, 1165–1179, <http://dx.doi.org/10.1111/j.1365-246X.2007.03415.x>
 1214
 1215 BIGGS, J., ANTHONY, E. Y. & EBINGER, C. J. 2009. Multiple
 1216 inflation and deflation events at Kenyan volca-
 1217 noes, East African Rift. *Geology*, **37**, <http://dx.doi.org/10.1130/G30133A.1>
 1218
 1219 BIGGS, J., MOTHES, P., RUIZ, M., AMELUNG, F., DIXON,
 1220 T. H., BAKER, S. & HONG, S.-H. 2010. Stratovolcano
 1221 growth by co-eruptive intrusion: the 2008 eruption of

1222 Tungurahua Ecuador. *Geophysical Research Letters*,
 1223 **37**, L21302.
 1224 BÜRGMANN, R., ROSEN, P. A. & FIELDING, E. J. 2000. Syn-
 1225 thetic aperture radar interferometry to measure Earth's
 1226 surface topography and its deformation. *Annual*
 1227 *Review of Earth and Planetary Sciences*, **28**, 169–209.
 1228 CARR, M. 1984. Symmetrical and segmented variation of
 1229 physical and geochemical characteristics of the
 1230 Central American volcanic front. *Journal of Volcanol-*
 1231 *ogy and Geothermal Research*, **20**, 231–252, [http://dx.doi.org/10.1016/0377-0273\(84\)90041-6](http://dx.doi.org/10.1016/0377-0273(84)90041-6)
 1232
 1233 EBMEIER, S. K., BIGGS, J., MATHER, T. A., WADGE, G. &
 1234 AMELUNG, F. 2010. Steady downslope movement on
 1235 the western flank of Arenal volcano, Costa Rica. *Geo-*
 1236 *chemistry, Geophysics, Geosystems*, **11**, Q12004,
 1237 <http://dx.doi.org/10.1029/2010GC003263>
 1238
 1239 EBMEIER, S. K., BIGGS, J., MATHER, T. A., ELLIOTT, J. R.,
 1240 WADGE, G. & AMELUNG, F. 2012. Measuring large
 1241 topographic change with InSAR: lava thicknesses,
 1242 extrusion rate and subsidence rate at Santiaguito
 1243 volcano, Guatemala. *Earth and Planetary Science*
 1244 *Letters*, **335–336**, 216–225, <http://dx.doi.org/10.1016/j.epsl.2012.04.027>
 1245
 1246 FERRETTI, A., PRATI, C. & ROCCA, F. 2001. Permanent
 1247 scatterers in SAR interferometry. *IEEE Transactions*
 1248 *on Geoscience and Remote Sensing*, **39**, 8–20.
 1249
 1250 FOSTER, J., BROOKS, B., CHERUBINI, T., SHACAT, C., BUS-
 1251 INGER, S. & WERNER, C. L. 2006. Mitigating atmos-
 1252 pheric noise for InSAR using a high resolution
 1253 weather model. *Geophysical Research Letters*, **33**,
 1254 16 304, <http://dx.doi.org/10.1029/2006GL026781>
 1255
 1256 FOURNIER, T. J., FREYMUELLER, J. & CERVELLI, P. 2009.
 1257 Tracking magma volume recovery at Okmok volcano
 1258 using GPS and an unscented Kalman filter. *Journal*
 1259 *of Geophysical Research*, **114**, B02405, <http://dx.doi.org/10.1029/2008JB005837>
 1260
 1261 FOURNIER, T. J., PRITCHARD, M. E. & RIDDICK, S. N. 2010.
 1262 Duration, magnitude, and frequency of subaerial
 1263 volcano deformation events: new results from Latin
 1264 America using InSAR and a global synthesis. *Geo-*
 1265 *chemistry, Geophysics, Geosystems*, **11**, 1003, <http://dx.doi.org/10.1029/2009GC002558>
 1266
 1267 FOURNIER, T., PRITCHARD, M. E. & FINNEGAN, N. 2011.
 1268 Accounting for atmospheric delays in InSAR data in
 1269 a search for long-wavelength deformation in South
 1270 America, *IEEE Trans. Geoscience and Remote*
 1271 *Sensing*, **99**, 1–12, <http://dx.doi.org/10.1109/TGRS.2011.2139217>
 1272
 1273 FRANSSON, J. E. S., SMITH, G. & ASKNE, J. 2001. Stem
 1274 volume estimation in boreal forests using ERS- 1/2
 1275 coherence and SPOT XS optical data. *International*
 1276 *Journal of Remote Sensing*, **22**, 2777–2791, <http://dx.doi.org/10.1080/01431160010006872>
 1277
 1278 GOLDSTEIN, R., ZEBKER, H. & WERNER, C. 1988. Satellite
 1279 Radar Interferometry: two dimensional phase unwrap-
 1280 ping. *Radio Science*, **23**, 713–720.
 1281
 1282 HAMLING, I. J., AYELE, A. ET AL. 2009. Geodetic obser-
 1283 vations of the ongoing Dabbahu rifting episode: new
 1284 dyke intrusions in 2006 and 2007. *Geophysical*
 1285 *Journal International*, **178**, 989–1003, <http://dx.doi.org/10.1111/j.1365-246X.2009.04163.x>
 1286
 1287 HANSEN, R. F. 2001. *Radar Interferometry Data*
 1288 *Interpretation and Error Analysis*. Kluwer Academic,
 1289 Dordrecht.

- 1219 HELENO, S. I. N., FRISCHKNECHT, C., D'OREYE, N., LIMA,
1220 J. N. P., FARIA, B., WALL, R. & KERVYN, F. 2010. Sea-
1221 sonal tropospheric influence on SAR interferograms
1222 near the ITCZ – The case of Fogo Volcano and
1223 Mount Cameroon. *Journal of African Earth Sciences*,
1224 **58**, 833–856, [http://dx.doi.org/10.1016/j.jafrearsci.](http://dx.doi.org/10.1016/j.jafrearsci.2009.07.013)
1225 2009.07.013
- 1226 JOLIVET, R., GRANDIN, R., LASSERRE, C., DOIN, M.-P. &
1227 PELTZER, G. 2011. Systematic InSAR tropospheric
1228 phase delay corrections from global meteorological
1229 reanalysis data. *Geophysical Research Letters*, **38**,
1230 L17311, <http://dx.doi.org/10.1029/2011GL048757>
- 1231 JÓNSSON, S., ZEBKER, H., SEGALL, P. & AMELUNG, F.
1232 2002. Fault slip distribution of the 1999 M w 7.1
1233 Hector Mine, California, earthquake, estimated from
1234 satellite radar and GPS measurements. *Bulletin of the*
1235 *Seismological Society of America*, **92**, 1377–1389.
- 1236 LI, Z., MULLER, J., CROSS, P. & FIELDING, E. J. 2005.
1237 Interferometric synthetic aperture radar (InSAR)
1238 atmospheric correction: GPS, Moderate Resolution
1239 Imaging Spectroradiometer (MODIS), and InSAR
1240 integration. *Journal of Geophysical Research (Solid*
1241 *Earth)*, **110**, B93410, [http://dx.doi.org/10.1029/](http://dx.doi.org/10.1029/2004JB003446)
1242 2004JB003446
- 1243 LI, Z., MULLER, J.-P., CROSS, P., ALBERT, P., FISCHER, J. &
1244 BENNARTZ, R. 2006. Assessment of the potential of
1245 MERIS near-infrared water vapour products to
1246 correct ASAR interferometric measurements. *Inter-*
1247 *national Journal of Remote Sensing*, **27**, 349–365,
1248 <http://dx.doi.org/10.1080/01431160500307342>
- 1249 LIN, Y.-N., SIMONS, M., HETLAND, E. A., MUSÈ, P. &
1250 DiCAPRIO, C. 2010. A multi-scale approach to estimat-
1251 ing topographically correlated propagation delays in
1252 radar interferometry. *Geochemistry, Geophysics, Geo-*
1253 *systems*, **11**, Q09002, [http://dx.doi.org/10.1029/](http://dx.doi.org/10.1029/2010GC003228)
1254 2010GC003228
- 1255 LIU, J. G., BLACK, A., LEE, H., HANAIZUMI, H. & MOORE,
1256 J. M. 2001. Land surface change detection in a desert
1257 area in Algeria using multi-temporal ERS SAR coher-
1258 ence images. *International Journal of Remote Sensing*,
1259 **22**, 2463–2477, [http://dx.doi.org/10.1080/01431160](http://dx.doi.org/10.1080/01431160152497673)
1260 152497673
- 1261 LIU, G., LI, J. ET AL. 2010. Surface deformation associated
1262 with the 2008 Ms8.0 Wenchuan earthquake from
1263 ALOS L-band SAR interferometry. *International*
1264 *Journal of Applied Earth Observation and Geoinfor-*
1265 *mation*, **12**, 496–505.
- 1266 LOHMAN, R. B. & SIMONS, M. 2005. Some thoughts on the
1267 use of InSAR data to constrain models of surface defor-
1268 mation: noise structure and data downsampling. *Geo-*
1269 *chemistry, Geophysics, Geosystems*, **6**, Q01007,
1270 <http://dx.doi.org/10.1029/2004GC000841>
- 1271 LU, Z. & DZURISIN, D. 2010. Ground surface deformation
1272 patterns, magma supply, and magma storage at Okmok
1273 volcano, Alaska, from InSAR analysis: 2. Coeruptive
1274 deformation July–August 2008. *Journal of Geophys-*
1275 *ical Research (Solid Earth)*, **115**, B00B03, [http://dx.](http://dx.doi.org/10.1029/2009JB006970)
1276 [doi.org/10.1029/2009JB006970](http://dx.doi.org/10.1029/2009JB006970)
- MARTINI, F., TASSI, F., VASELLI, O., DEL POTRO, R., MAR-
TINEZ, M., VAN DEL LAAT, R. & FERNANDEZ, E. 2010.
Geophysical, geochemical and geodetical signals of
reawakening at Turrialba volcano (Costa Rica) after
almost 150 years of quiescence. *Journal of Volcanol-*
ogy and Geothermal Research, **198**, 416–432,
<http://dx.doi.org/10.1016/j.jvolgeores.2010.09.021>
- MASSONNET, D. & FEIGL, K. L. 1995. Discrimination
of geophysical phenomena in satellite radar inter-
ferograms. *Geophysical Research Letters*, **22**,
1537–1540, <http://dx.doi.org/10.1029/95GL00711>
- MASSONNET, D. & FEIGL, K. L. 1998. Radar interferom-
etry and its application to changes in the Earth's surface.
Reviews of Geophysics, **36**, 441–500.
- MASSONNET, D., BRIOLE, P. & ARNAUD, A. 1995. Defla-
tion of Mount Etna monitored by spaceborne radar
interferometry. *Nature*, **375**, 567–570, [http://dx.doi.](http://dx.doi.org/10.1038/375567a0)
[org/10.1038/375567a0](http://dx.doi.org/10.1038/375567a0)
- PAVEZ, A., REMY, D. ET AL. 2006. Insight into ground
deformations at Lascar volcano (Chile) from SAR
interferometry, photogrammetry and GPS data: impli-
cations on volcano dynamics and future space monitor-
ing. *Remote Sensing of Environment*, **100**, 307–320,
<http://dx.doi.org/10.1016/j.rse.2005.10.013>
- PHILIBOSIAN, B. & SIMONS, M. 2011. A survey of volcanic
deformation on Java using ALOS PALSAR interfero-
metric time series. *Geochemistry, Geophysics, Geo-*
systems, **12**, Q11004, [http://dx.doi.org/10.1029/2011](http://dx.doi.org/10.1029/2011GC003775)
[GC003775](http://dx.doi.org/10.1029/2011GC003775)
- PINEL, V., HOOPER, A., DE LA CRUZ-REYNA, S., REYES-
DAVILA, G., DOIN, M. P. & BASCOU, P. 2011. The chal-
lenging retrieval of the displacement field from InSAR
data for andesitic stratovolcanoes: case study of Popo-
catepetl and Colima Volcano, Mexico. *Journal of Vol-*
canology and Geothermal Research, **200**, 49–61,
<http://dx.doi.org/10.1016/j.jvolgeores.2010.12.002>
- PRITCHARD, M. E. & SIMONS, M. 2004. An InSAR-based
survey of volcanic deformation in the central Andes.
Geochemistry, Geophysics, Geosystems, **5**, Q02002,
<http://dx.doi.org/10.1029/2003GC000610>
- REMY, D., BONVALOT, S., BRIOLE, P. & MURAKAMI, M. .
2003. Accurate measurements of tropospheric effects
in volcanic areas from SAR interferometry data: appli-
cation to Sakurajima volcano (Japan). *Earth and Plan-*
etary Science Letters, **213**, 299–310, [http://dx.doi.](http://dx.doi.org/10.1016/S0012-821X(03)00331-5)
[org/10.1016/S0012-821X\(03\)00331-5](http://dx.doi.org/10.1016/S0012-821X(03)00331-5)
- REUTER, H., NELSON, A., STROBL, P., MEHL, W. & JARVIS,
A. 2009. A first assessment of ASTER GDEM tiles for
absolute accuracy, relative accuracy and terrain par-
ameters. In: *Geoscience and Remote Sensing Sym-*
posium, 2009. IGARSS '09. IEEE International,
Volume 5. Institute of Electrical and Electronics Engi-
neers (IEEE), Piscataway, NJ, 240–243, [http://dx.doi.](http://dx.doi.org/10.1109/IGARSS.2009.5417688)
[org/10.1109/IGARSS.2009.5417688](http://dx.doi.org/10.1109/IGARSS.2009.5417688)
- RODRIGUEZ, E. & MARTIN, J. M. 1992. Theory and design
of interferometric synthetic aperture radars. *IEE Pro-*
ceedings: Radar and Signal Processing, **139**,
147–159.
- RODRIGUEZ, E., MORRIS, C. S. & BEIZ, J. E. 2006. A global
assessment of the SRTM performance. *Photogram-*
metric Engineering and Remote Sensing, **72**, 249–260.
- ROSEN, P., HENSLEY, S., ZEBKER, H., WEBB, F. & FIELD-
ING, E. 1996. Surface deformation and coherence
measurements of Kilauea volcano, Hawaii, from

- 1277 SIR-C radar interferometry. *Journal of Geophysical*
 1278 *Research*, **101**, 23 109–23 125.
- 1279 ROSEN, P., HENSLEY, S., GURROLA, E., ROGEZ, F., CHAN,
 1280 S., MARTIN, J. & RODRIGUEZ, E. 2001. SRTM C-band
 1281 topographic data: quality assessments and calibration
 1282 activities. In: *Geoscience and Remote Sensing Sym-*
 1283 *posium, 2001. IGARSS '01. IEEE 2001 International,*
 1284 *Volume 2.* Institute of Electrical and Electronics Engin-
 1285 eers, Piscataway, NJ, 739–741, <http://dx.doi.org/10.1109/IGARSS.2001.976620>
- 1286 ROSEN, P. A., HENSLEY, S., PELTZER, G. & SIMONS, M .
 1287 2004. Updated repeat orbit interferometry package
 1288 released. *EOS, Transactions of the American Geophy-*
 1289 *sical Union*, **85**, 47.
- 1290 SANTORO, M., ASKNE, J., SMITH, G. & FRANSSON, J. E. S.
 1291 2002. Stem volume retrieval in boreal forests from
 1292 ERS-1/2 interferometry. *Remote Sensing of Environ-*
 1293 *ment*, **81**, 19–35, ISSN 0034-4257, [http://dx.doi.org/10.1016/S0034-4257\(01\)00329-7](http://dx.doi.org/10.1016/S0034-4257(01)00329-7)
- 1294 SCHMIDT, D. A. & BÜRGMANN, R . 2003. Time-dependent
 1295 land uplift and subsidence in the Santa Clara valley,
 1296 California, from a large interferometric synthetic
 1297 aperture radar data set. *Journal of Geophysical*
 1298 *Research*, **108**, 2416, <http://dx.doi.org/10.1029/2002JB002267>
- 1299 SEYMOUR, M. & CUMMING, I. 1994. Maximum likelihood
 1300 estimation for SAR interferometry. In: *Geoscience*
 1301 *and Remote Sensing Symposium, 1994. IGARSS '94.*
 1302 *Surface and Atmospheric Remote Sensing: Technol-*
 1303 *ogies, Data Analysis and Interpretation. IEEE Inter-*
 1304 *national, Volume 4.* Institute of Electrical and
 1305 Electronics Engineers, Piscataway, NJ, 2272–2275,
 1306 <http://dx.doi.org/10.1109/IGARSS.1994.399711>
- 1307 SHIRZAEI, M. & BÜRGMANN, R . 2012. Topography corre-
 1308 lated atmospheric delay correction in radar interfero-
 1309 metry using wavelet transforms. *Geophysical*
 1310 *Research Letters*, **39**, L01305, <http://dx.doi.org/10.1029/2011JGL049971>
- 1311 STEVENS, N. F. & WADGE, G. 2004. Towards operational
 1312 repeat-pass SAR interferometry at active volcanoes.
 1313 *Natural Hazards*, **33**, 47–76, <http://dx.doi.org/10.1023/B:NHAZ.0000035005.45346.2b>
- 1314 STEVENS, N. F., WADGE, G., WILLIAMS, C. A., MORLEY,
 1315 J. G., MULLER, J., MURRAY, J. B. & UPTON, M .
 1316 2001. Surface movements of emplaced lava flows
 1317 measured by synthetic aperture radar interferometry.
 1318 *Journal of Geophysical Research*, **106**, 11 293–
 1319 11 314, <http://dx.doi.org/10.1029/2000JB900425>
- 1320 WADGE, G., WEBLEY, P. W. ET AL. 2002. Atmospheric
 1321 models, GPS and InSAR measurements of the tropo-
 1322 spheric water vapour field over Mount Etna. *Geophys-*
 1323 *ical Research Letters*, **29**, 190, <http://dx.doi.org/10.1029/2002GL015159>
- 1324 WADGE, G., MATTIOLI, G. S. & HERD, R. A. 2006. Ground
 1325 deformation at Soufriere Hills Volcano, Montserrat
 1326 during 1998–2000 measured by radar interferometry
 1327 and GPS. *Journal of Volcanology and Geothermal*
 1328 *Research*, **152**, 157–173, <http://dx.doi.org/10.1016/j.jvolgeores.2005.11.007>
- 1329 WADGE, G., ZHU, M., HOLLEY, R. J., JAMES, I. N., CLARK,
 1330 P. A., WANG, C. & WOODAGE, M. J. 2010. Correction
 1331 of atmospheric delay effects in radar interferometry
 1332 using a nested mesoscale atmospheric model. *Journal*
 1333 *of Applied Geophysics*, **72**, 141–149.
- 1334 WEBLEY, P. 2004. Determining radio wave delay by non-
 hydrostatic atmospheric modelling of water vapour
 over mountains. *Physics and Chemistry of the Earth*,
29, 139–148, <http://dx.doi.org/10.1016/j.pce.2004.01.013>
- WICKS, C. W., DZURISIN, D., INGEBRITSEN, S., THATCHER,
W., LU, Z. & IVERSON, J. 2002. Magmatic activity
beneath the quiescent Three Sisters volcanic center,
central Oregon Cascade Range, USA. *Geophysical*
Research Letters, **29**, 070, <http://dx.doi.org/10.1029/2001GL014205>
- ZEBKER, H. A. & VILLASENOR, J. 1992. Decorrelation in
interferometric radar echoes. *IEEE Transactions on*
Geoscience and Remote Sensing, **30**, 950–959,
<http://dx.doi.org/10.1109/36.175330>
- ZEBKER, H. A., ROSEN, P. A. & HENSLEY, S. 1997. Atmos-
pheric effects in interferometric synthetic aperture
radar surface deformation and topographic maps.
Journal of Geophysical Research, **102**, 7547–7564,
<http://dx.doi.org/10.1029/96JB03804>
- ZEBKER, H., AMELUNG, F. & JONSSON, S. 2000. Remote
sensing of volcano surface and internal processing
using radar interferometry. In: MOUGINIS-MARK, P.,
CRISP, J. & FINK, J. (eds) *Remote Sensing of Active Vol-*
canism. American Geophysical Union, Geophysical
Monograph, **116**, 179–205.

